NTNU
Norwegian University of
Science and Technology

Multicopter Attitude Estimation with North-Seeking Capabilities

Pål Holthe Mathisen

Master of Science in Cybernetics and Robotics

Submission date:	June 2018
Supervisor:	Thor Inge Fossen, ITK
Co-supervisor:	Kristian Klausen, ITK

Norwegian University of Science and Technology
Department of Engineering Cybernetics

NTNU
Norwegian University of
Science and Technology

Faculty of Information Technology
and Electrical Engineering
Department of Engineering Cybernetics

MSC THESIS DESCRIPTION SHEET

Name:	Pål Holthe Mathisen
Department:	Engineering Cybernetics
Thesis title:	Multicopter Attitude Estimation with North-Seeking Capabilities

Thesis Description:

The goal of the project is to develop an attitude estimator for a multicopter operating with a sensor package consisting of an IMU (gyros and accelerometers) and position aiding. This is motivated by a lack of published literature on methods providing cheap North-seeking heading measurements for multicopters.

The following items should be addressed:

1. Literature study and review of multicopter attitude estimation.
2. Create a simulation environment of the entire system, capable of visualizing the flight. This is to be used to test different algorithms.
3. Investigate, develop and discuss methods for measurement of roll and pitch using available sensory packages.
4. Investigate, develop and discuss methods for measurement of heading angle using state-of-the-art sensory packages
5. Verify performance of methods by computer simulations in a realistic multicopter-inspection scenario.
6. Conclude your findings in a report. Include Matlab/C-code as digital appendices.

Start date:	2018-01-08
Due date:	2018-06-04

Thesis performed at:	Department of Engineering Cybernetics, NTNU
Supervisor:	Professor Thor I. Fossen, Dept. of Eng. Cybernetics, NTNU
Co-Supervisor:	Dr. Kristian Klausen, Dept. of Eng. Cybernetics, NTNU

Preface

This work is carried out at the Department of Engineering Cybernetics, the spring of 2018. The process had Professor Thor Inge Fossen, as main supervisor and Doctor Kristian Klausen, CTO of Scout Drone Inspection, as the co-supervisor.

In the beginning, the purpose of this thesis was to provide navigation-, control- and aerial robotics solutions for specific problems faced by the company Scout Drone Inspection. It involved creating a simulation environment where testing of different algorithms and maneuver, and development of said algorithms and maneuvers could happen in a realistic scenarios. As time progressed, it became clear that a better end product would be achieved if the task focused solely on navigation solutions. Thus, the focus for the thesis became attitude measurement solutions for multicopters.

At the beginning of the semester I had a partially functional simulator and autopilot to work with, capable of moving at low accelerations and velocities. The methods developed for attitude measurements needed high accelerations, so much time in the early stages of the thesis was spent on implementing a visualization tool. The purpose of the tool was to get a better understanding of what kind of tuning the autopilot needed to achieve high accelerations without losing control of the multicopter. All of the code used for simulations is written by me, while a sizable portion of the code for the autopilot and multicopter simulator comes from my previous work. All work was done in MatLab2017 and for the virtual results, no confidential information was provided.

For the experimental results, I was provided with processed data by Kristian Klausen. This data comes from indoor flights by a 4-rotor multicopter (picture of multicopter provided in the Chapter 5) inside the department's Motion-Capture Laboratory. This laboratory provided high-accuracy position measurements through 16 imaging sensors, which is needed for position aiding in all the developed solutions.

Acknowlegment

There are many people I want to credit for their help with this thesis. First of all, I would like to thank my family. They have helped me with motivation, guidance on technical matters and reviewing my written work. It is safe to say my days this spring would have been much harder without their support.

I would also direct my gratitude towards my supervisor, Thor Inge, and co-supervisor, Kristian, for their guidance on both technical matters and academic writing. Looking back at how much I have learned over the past year under their supervision, I am thankful for them introducing me to academic work, for always finding time when I needed advice, and for coming up with suggestions leading to the progression in my work whenever I was stuck.

At last, I would like to send my regards to my office mates that have created a wonderful working environment, to my other colleagues that I always could discuss my work with and draw upon for inspiration. A special thanks is also sent towards NTNU Post.doc Torleiv Håland Bryne and Dr. Kenneth Gade, a researcher at FFI within navigation, who both took their time explaining certain principles within vehicle navigation and helped finding relevant literature.

Trondheim, June 22, 2018
Pål Holthe Mathisen

Abstract

This thesis deals with attitude measurement by fusing sensor information from accelerometers, gyros and position aiding in the form of a pseudorange measurement system, on a multicopter system. This is motivated by multicopter being highly accelerated systems, meaning that the acceleration vector is a reliable choice for heading measurements. Estimation of roll and pitch using the gravity vector in a non-accelerated environment is also tested. The sensor fusion is mostly done on data from a simulated multicopter, meaning that nothing could directly be said about the heading angle from knowledge of the vehicle's velocity in the body-frame. Three different approaches to the heading measurements is investigated, all which performs an averaging of the heading measurements over specific time intervals to minimize random deviations from the true value. The methods all compare the acceleration vector from the accelerometer measurements, compensated for roll and pitch, with either the actual acceleration vector or a substitute, in NED-frame obtained by the position aiding system. The achieved accuracy of the best averaged measurement method in the simulated environment is on average $0.21°$. The best results for the method not dependent on initial conditions and specific motion achieves an averaged accuracy of $3.26°$. The simulated results were found through the use of the Monte Carlo method.

Experimental results from real multicopter flight data were less promising. The best results showed about $7° - 8°$, and are not surprisingly from the method requiring no additional conditions, as a real manual flight has less control of the motion than an autopilot.

The thesis concludes that all methods require a sufficient level of acceleration to observe the heading with any accuracy. Since high acceleration is required reliable heading, while low acceleration is required for reliable roll and pitch, the two measurements should not be performed at the same time.

The method of finding the time interval over which to average the heading measurements should also be improved further, as significant errors occur at non-zero heading angles for the current setup.

Sammendrag

Denne oppgaven undersøker attitude måling ved bruk av kombinert sensorinformasjon fra akselerometre, gyroskoper og posisjonskorreksjon i form av et avstandsmålesystem, på et multikopter. Motivasjonen for dette er at multikoptre er systemer som opererer med høyer akselerasjoner, som betyr at akselerasjonsvektoren er godt egnet til pålitelig å måle giringsrotasjon. Rull- og pitchestimering ved bruk av gravitasjonsvektoren er også testet i ikke-akselererte situasjoner. Kombineringen av sensordata gjøres for det meste med data fra et simulert multikopter, som betyr at kunnskap om fartøyets hastighet dekomponert i body-systemet ikke direkte gir informasjon om dets giringsvinkel. Tre forskjelligen fremgangsmåter for giringsestimering er undersøkt. Alle utfører en midling av måleresultatene over spesifikke tidsintervall for å redusere hvitstøysavvik fra den virkelige verdien. Alle metodene sammenligner akselerasjonsvektoren fra akeslerometermålingene, kompensert for påvirkning fra rull og pitch, med enten akselerasjonsvektoren eller en tilsvarende vektor med riktige kvaliteter, i NED-systemet. Vektorene i NED-systemet finnes gjennom avstandsmålesystemet. Den beste simulerte metoden oppnår en gjennomsnittlig nøyaktighet på 0.21°. Beste resultat for metoden uten antagelser om initialtilstand og bevegelse oppnår gjennomsnittlig nøyaktighet på 3.26°. Alle simulerte resultater er funnet ved bruk av Monte Carlo-metoden.

For å teste nøyaktighet utenfor et simuleringsmiljø er flyvning av et virkelig multikopter gjort. De eksperimentelle resultatene er ujje kuje lovende, og oppnår kun nøyaktighet på $7° - 8°$. Det er ikke overraskende at metoden uten tilleggskrav for initialtilstand og bevegelser er den beste, siden manuell kontroll av flyvningen vil følge disse kravene dårligere enn en autopilot.

Oppgaven konkluderer med at alle metodene trenger en akselerasjonsvektor av tilstrekkelig lengde for å kunne observere giringsvinklen. Siden høy akselerasjon er påkrevd får pålitelige giringsmålinger, og lav akselerasjon for pålitelige rull- og pitch-vinkler er det åpenbart at disse to målingene ikke kan utføres samtidig. Metoden for å finne tidsintervallet som giringsmålingene midles over burde utvikles videre, siden nåværende oppsett opplever at betydelige estimeringsfeil oppstår når målingene ikke utfåres med giringsvinkel lik null.

Contents

Chapter 1

Introduction

The purpose of modern navigation systems is usually to estimate the state of a craft of vehicle by the six degrees of freedom within a required accuracy. Throughout the history, navigation has mainly been about getting from one place to another over larger distances. In the ancient and medieval world, the fastest way to traverse great distances was by ship. This explains the etymology of the word "navigation", which through several translations has its root in the Latin words *navis*, "ship", and *agere*, "to set in motion" (Harper, 2018).

1.1 Background

The most common ways to navigate in pre-modern times were either by moving relative to known geography, to use primitive versions of the compass or to navigate using celestial bodies. Various breakthroughs in technology has made navigation more reliable over the centuries, like the Vikings utilizing the sunstone to locate the sun in a completely overcast sun, or when the sextant were introduced around the 17th century, allowing for more accurate measurements of star positions. Another important breakthrough came when Anschutz invented the gyrocompass in 1908, before the "father of modern navigation" (Public Broadcasting Service, 2018), Elmer Ambrose Sperry, in parallel invented and patented it in 1911 (Sperry, 1911). As more and more ships (still the primary method of transportation) during the 1800's were made from metal rather than wood, the field lines that the magnetic compass measures were disturbed, rendering it less accurate and paving the way for the gyrocompass and entry into modern navigation.

In early modern navigation, gimbals were the main way of mounting systems. They relied on gimbal inertial sensor technology and physical self-alignment to recieve information about attitude. However as the digital age arrived, the gimbal systems received competition by the new strapdown systems, that compensated the loss of attitude information by introducing rate gyros, measuring angular velocity at extremely high frequencies to find attitude. The strapdown systems removed the need for some calibration, reduced cost and weight, while also completely eliminates gimbal lock. As digital technology progressed, the cost, size and weight of strapdown system plummeted to a point where the gimbal based systems no longer were a viable option.

Navigation is becoming increasingly important today, where it is not only used to navigate to places outside visual range, but also to provide state information to autonomous systems. Micro-electro-mechanical (MEMs) inertial navigation systems (INS) has become so affordable that they are placed in almost every smart-phone and autonomous craft, with the accuracy of their estimates being limited mainly by price.

1.2 Motivation

Most navigation systems today contains at least a basic inertial measurement unit (IMU), consisting of an accelerometer for each transitional degree of freedom and a rate gyro for each rotational degree of freedom. They navigate using dead reckoning, which is calculating position and attitude base on measuring their derivatives over time. Such methods is also often called inertial navigation, and is subject to cumulative errors originating both in integrated biases and in resolution error, i.e. error from not being a continuous system. These cumulative errors need to be corrected for, which leads to aided inertial navigation systems (AINS).

AINS introduces the concept of sensor fusion, which combines a standard INS with complementing sensors that capable of correcting cumulative errors from the IMU. The standard example for position and velocity error correction would be a GNSS. There are however many other sensor packages that could provide position aiding, like systems capable of simultaneous localization and mapping (SLAM) or local range-based systems. While systems able to measure position in theory also provides observability to velocity and acceleration, it cannot compete with the IMU's accuracy of the dynamics, as it takes time to accurately find acceleration from position measurements due to measurement noise being amplified by differentiation.

Complementing measurement methods for attitude are not as standardized as the GNSS. There exists a many methods, and as the observability of the attitude for each method depends on both the environment in which the craft is situated and the dynamics of the craft, it is not always that straight forward. For roll and pitch, mankind is blessed with the ever-present gravity force that is well documented and mapped, which allows the two angles to be observed accurately whenever the craft remains non-accelerated. The last rotational DoF however is another story, which is thoroughly described in both 4.3.1.

Measuring heading indirectly by comparing the acceleration vector in NED-system and body-system is a method that is easily available with basic sensors for inertial navigation, while also preferable for highly accelerated systems like multicopters. Using the acceleration vector is also advantageous as the movement of multicopter systems are not restricted by heading, meaning that every vector in body-system has to be measured.

1.3 Contribution

This thesis investigates different methods for measuring heading during flight for multi-rotor UAV's. It goes into detail on three different approaches of acceleration based heading aiding. These are comparing the acceleration vector measured by accelerometers to translational vectors in inertial frame estimated through the position aiding sensors. The thesis also makes use of gravity measured by the accelerometers for estimating roll- and pitch-angles. The heading measurement methods are also tested using experimental data from flight done by a real-life multicopter UAV.

For all methods, results will show accuracy when simulated in an ideal simulation environment, free of disturbances and restrictions. A specific maneuver is developed which ensures enough acceleration to observe the heading angle over time, and then averages the measurements to provide a single measurement of higher accuracy.

Finally, the possibility of using any of the methods in a realistic UAV operation is discussed. The methods will be compared with each other by their complexity of implementation, accuracy of attitude estimates and their measurement reliability.

1.4 System Restrictions

Some assumptions about the environment of which the multicopter operates have been made.

The autopilot is assumed know the attitude for the attitude controllers to a reasonable degree. This is a reasonable assumption as gyroscopes are available, and the angle calibration is suppose to happen before the angle estimates are allowed to drift too much.

The attitude is also assumed to be between $\pm\frac{\pi}{2}$ for roll and pitch, as it otherwise is unable to compensate for gravity.

Assumption 1: The angles ϕ and θ is assumed to be within the values $\pm\frac{\pi}{2}$ at all time

The multicopter is also assumed to fly in perfect conditions. This means no air resistance, wind or other disturbances unmodeled by the autopilot, as this project is only meant to show a proof of concept, not necessarily test the methods' robustness.

The presence of clock biases in pseudorange measurements systems is well know. However, as this project is focusing on the attitude estimation, the clock bias is omitted to simplify the system. This means that the pseudorange measurement system is only perturbed by the Gaussian white noise and is otherwise perfect.

If the vehicle system should always be able to compensate for the gravity force, a saturation has to be made on the desired horizontal acceleration. The length of the desired acceleration in the horizontal directions should not exceed a certain amount. This amount is limited by the maximum rotor output, r_{max}, of the multicopter, and if found by calculating the maximum roll/pitch angle combination that still gives r_{max} decomposed in vertical direction larger than the gravitational pull.

This restriction on the acceleration causes an additional need for a restriction on the velocity as well. This is because a saturation on the acceleration will restrict the multicopter's ability to break rapidly.

1.5 System description

The system consists of three major parts. Autopilot, state estimator with sensor models and attitude measuring algorithms, and a multicopter imitating real physical dynamics. The flow chart for information flow between the system parts is illustrated in Figure 1.1. The in-depth description of each part if found in the Chapters numbered by Figure 1.1.

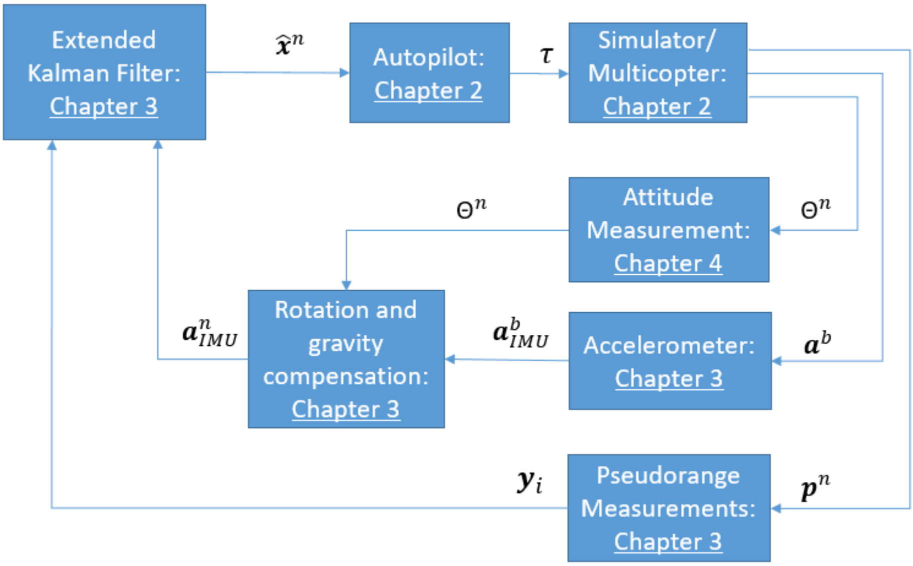

Figure 1.1: System information flow chart

The system will operate mainly in two different reference frames, however, two additional reference frames are introduced to explain certain concepts:

- The North-Est-Down-frame (NED), denoted $\{n\}$, is used as the geographically stationary frame. Its origin is places either at a fixed point near the vehicle starting position or the starting position itself. Its axes are defined such that the x-axis always points towards the north, the z-axis points normal to the plane tangential to the vehicle's current position and the y-axis is complementing the x- and z-axes to form a right handed coordinate system. As the system in use is operating in proximity to its starting position, no updates is made online to the NED-frame.

- The body-frame, denoted $\{b\}$, is the body fixed, body centered reference frame which movements and rotations defines the movement and rotations of the vehicle. Its origin is usually placed at the center of mass of the vehicle. Its x-axis will in the case for ships and planes point in the vehicle's forward direction, but for a multicopter no such direction exists. For the system in use, the z-axis is defined in the direction the rotors forces air, while the x-axis is chosen such that expressions for torque control is simplified. The y-axis is complementing the x- and z-axes to form a right handed coordinate system.

- The ECEF-frame, or Earth Centered Earth Fixed, denoted $\{e\}$, is sometimes mentioned, as some methods is relying upon the rotation of the Earth. It has its origin centered at the center of the Earth, its z-axis aligned with the True North (Earth's axis of rotation), the x-axis pointing towards the reference meridian (zero longitude) and the y-axis is complementing a right hand system.

- The ECI-frame, or Earth Centered Inertial, denoted $\{i\}$, is sometimes mentioned for the same reasons as the ECEF-frame. It has its origin centered at the center of the Earth, its z-axis aligned with the True North (Earth's axis of rotation), the x-axis is pointing towards the sun during the vernal equinox and the y-axis is complementing a right hand system.

It should be noted that compared to most literature, the NED-frame is used as the global frame instead of the ECEF-frame.

1.6 Literature

This sections focuses on what literature this thesis builds upon. It is divided into topics of appropriate coherence.

1.6.1 Simulator, autopilot and state estimator

Simulation and modeling of multicopter

The multicopter simulator was constructed using models from the early parts of (Klausen, 2017), which in turn was based on (Fossen, 2011). It provided a simple simulation model with sufficient realism and had the advantage of also partially covering the control methods for said model. (Egeland and Gravdahl, 2002) provided discussion about different simulation methods, which in particular became relevant for a system with a pure integrator.

Control scheme

Once again, the control scheme is based on work done in (Klausen, 2017). The control allocation for desired angles is taken directly from his work, while the PD-controllers are not. The method of choosing the relative regulator gains was crucial for the stability of the transitional-attitude controlling dynamics and is primarily based upon information found in (Beard and McLain, 2012) on the chapter involving the method of successive loop closure. Inspiration to a suggested method of combating the chattering caused by the speed limitations was taken from sliding mode control's method of dealing with it, found in (Fossen, 2011).

Sensor models

For modeling of realistic state estimation, sensor models had to be introduced. Specifically, a model for accelerometers and a model for a pseudorange measurement system needed to be defined. (Farrell, 2008) was an excellent source for aided inertial navigation, and provided a good model for the accelerometer that modeled both a static measurement error in form of a bias, and a zero-mean measurement noise to simulate changing errors.

The pseudorange measurement model used is similar to that of GNSS. It is a wide spread model which is found many places in the literature, but it was first encountered in (Johansen and Fossen, 2016), so a modified version of that model fitting the assumptions was used.

Kalman Filtering

For a project heavily focused on the state estimation with the help of Kalman filtering, there was need for a better understanding of the Kalman filtering method. (Brown and Hwang, 2012) had an excellent derivation of the linear Kalman filter, focusing on the journey from a standard state-space observer to the optimal observer with regards to estimation error variance, given certain conditions. (Farrell, 2008) provided a link between the least-square, recursive least-square and Kalman filter method. (Vik, 2014) was a good support literature that explained certain areas more thoroughly, better for entry-level readers. Together, they gave different perspectives to the challenges when applying the extended Kalman filter to nonlinear systems.

When analyzing the observability of the system, (Johansen et al., 2017) was a source for explaining some parts of the derivation. The understanding of the requirement of linear independence between the different pseudorange measurement vectors was supported by the book on system identification and adaptive control, (Ioannou and Sun, 2012). It contained a detailed description about how input information must have sufficient rank to be able to estimate system parameters, often through pseudo-inverses.

1.6.2 Attitude estimation

1.6.3 Pitch- and roll estimation

The method of estimating roll- and pitch angles by exploiting that the gravity vector is known in NED-frame, is an well documented one. It mentioned briefly in (Gade, 2016), but both theory and approach is explained in detail in (Fossen, 2011, Chapter 11.5).

1.6.4 Heading estimation

As heading estimation was the focus of this thesis, it was also where most time were spent going through the literature. A complete overview of all the different fundamental ways of measuring heading is provided by (Gade, 2016). This paper states the 7 different vector one could measure to estimate the heading angle, as well as their respective strengths and weaknesses. At the same time, it formulates a first order approximation of how the measurement error from measuring the vector propagates to the estimation error.

The notation when working with vectors and matrices in many different coordinate frames is hard to keep track on. The system introduced in (Gade, 2010) is an unambiguous notation system for transforming between the different coordinate frames used in navigation.

As for previous work on the area, (No et al., 2014) investigates sensor fusion of accelerometers, GPS and magnetometers for aiding attitude estimates on small UAVs. They discovered acceleration of body gave inaccurate roll- and pitch-measurements, which in turn propagated as error in heading angle output from the magnetometers. this caused them to omit the accelerometers as a heading aiding source.

Acceleration aided heading estimation was also attempted in (Hemerly et al., 2012) with the aiding of a GPS-system capable of measuring both position and velocity. They achieved a heading estimate of high accuracy, with increasing accuracy for higher speeds.

1.7 Notation

The Euclidean vector norm will be often used to find geometric distances, and is denoted $\|\cdot\|_2$. The transpose of a vector or matrix is denoted with $(\,\cdot\,)^T$. Reference frames are noted by $\{\,\cdot\,\}$. The $n \times n$ identity matrix is denoted $\boldsymbol{I}_n$ and $(\,\cdot\,)_{n\times m}$ is an $n \times m$ matrix filled with $(\,\cdot\,)$. The $\boldsymbol{S}(\,\cdot\,)$ operator produces a 3×3 square skew-symmetric matrix, as explained in Appendix A.3. A coordinate vector has different element values decomposed in different reference frames, so to explicitly state that a vector is decomposed in frame $\{a\}$, a vector v is written v^a.

1.8 Abbreviations

The following abbreviations used means:

INS - Inertial Navigation System
AINS - Aided Inertial Navigation System
DoF - Degree of Freedom
IMU - Inertial Measurment System
PVA - Position, Velocity, Accelereation
UAV - Unmaned Aerial Vehicle
GNSS - Global Navigation Satellite System
GAS - Globally Asymptoticlly Stable
GES - Globally Exponentially Stable
LFC - Lyapynov Function Candidate
NED - North East Down
MEMS - Micro-electro-mechanical system
SLAM - Simultanious Localization and Mapping

Chapter 2

Simulation Model

The following chapter will explain the structure of the multicopter model and its autopilot. The word "Multicopter" is referring to an unmanned drone helicopter with four or more propellers. A simulation environment, vehicle model and control system has to be created in order to test the more specific methods for vehicle navigation. Both the multicopter model and its control system is heavily based upon (Klausen, 2017).

The development of the simulator was started during a previous project thesis, but has since been improved in terms of functionality and performance. All code is written in MatLab, with the exception of support functions from (Fossen and Perez, 2004). Code could be found in Appendix E.

2.1 Simulation Environment

As the environment in which the multicopter is to operate is unspecified, the system will take no concern modeling obstacles or other environmental restrictions. As far as the multicopter is aware, it maneuvers in an infinite, empty void with only eight range transponders at fixed positions around. No external forces will influence the quadcopter except for gravity and the vehicle is modeled as a rigid body in six degrees of freedom. For the purpose of this project the earthly rotation has a negligible effect on the system. Combining this with the fact that the multicopter will stay close to its geographic starting area, it is reasonable to assume that NED-frame is inertial. It will therefore only be used two reference frames, NED($\{n\}$) frame and body($\{b\}$) frame, specified in Section 1.5.

2.2 Multicopter Model

The multicopter UAV model in use assumes a perfect symmetric body about all axes, and has six degrees of freedom:

$$\boldsymbol{\eta} = \begin{bmatrix} \boldsymbol{\eta}_1 \\ \boldsymbol{\eta}_2 \end{bmatrix} = \begin{bmatrix} \boldsymbol{p}^n \\ \boldsymbol{\Theta} \end{bmatrix} \tag{2.1}$$

where $\boldsymbol{p} \in \mathbb{R}^3$ is the UAV's position in the inertial NED frame $\{n\}$, while $\Theta \in \mathbb{R}^3$ represents the attitude of the UAV's axes in the body frame $\{b\}$, relative to the axes of $\{n\}$.

The notation used for the linear and angular velocities:

$$\boldsymbol{\nu} = \begin{bmatrix} \boldsymbol{\nu}_1 \\ \boldsymbol{\nu}_2 \end{bmatrix} = \begin{bmatrix} \boldsymbol{v}^b \\ \boldsymbol{\omega}^b \end{bmatrix} \tag{2.2}$$

Where $\boldsymbol{v} \in \mathbb{R}^3$ is the linear velocity of the vehicle in $\{n\}$, while $\boldsymbol{\omega}^b \in \mathbb{R}^3$ is the angular velocities around the axes of $\{b\}$

To comprehend the dynamics of the system, it is essential to understand that not all these variables are given in the inertial frame. This is important since it is desirable to represent the states of the system, η, in $\{n\}$.

The dynamics of the system is the following

$$\begin{gathered}\dot{\boldsymbol{\eta}} = \boldsymbol{J}_{\Theta}\boldsymbol{\nu} \\ \Updownarrow \\ \begin{bmatrix}\dot{\boldsymbol{p}^n} \\ \dot{\boldsymbol{\Theta}}\end{bmatrix} = \begin{bmatrix}\boldsymbol{R}_b^n(\boldsymbol{\Theta}) & \mathbf{0}_{3\times 3} \\ \mathbf{0}_{3\times 3} & \boldsymbol{T}(\boldsymbol{\Theta})\end{bmatrix}\begin{bmatrix}\boldsymbol{v}^b \\ \boldsymbol{\omega}^b\end{bmatrix}\end{gathered} \tag{2.3}$$

and

$$\begin{gathered}\boldsymbol{M}\dot{\boldsymbol{\nu}} + \boldsymbol{C}\boldsymbol{\nu} + \boldsymbol{G}^b = \boldsymbol{\tau}_A \\ \Updownarrow \\ \begin{bmatrix}m_c\boldsymbol{I}_3 & \mathbf{0}_{3\times 3} \\ \mathbf{0}_{3\times 3} & \boldsymbol{I}_b\end{bmatrix}\begin{bmatrix}\dot{\boldsymbol{v}}^b \\ \dot{\boldsymbol{\omega}}^b\end{bmatrix} + \begin{bmatrix}m_c\boldsymbol{S}(\boldsymbol{\omega}^b) & \mathbf{0}_{3\times 3} \\ \mathbf{0}_{3\times 3} & -\boldsymbol{S}(\boldsymbol{I}_b\boldsymbol{\omega}^b)\end{bmatrix}\begin{bmatrix}\boldsymbol{v}^b \\ \boldsymbol{\omega}^b\end{bmatrix} + \begin{bmatrix}m_c\boldsymbol{g}^b \\ \mathbf{0}_{3\times 1}\end{bmatrix} = \begin{bmatrix}\boldsymbol{f}^b \\ \boldsymbol{M}\end{bmatrix}\end{gathered} \tag{2.4}$$

where $\boldsymbol{\tau}_A$ are the external forces that affects the system (gravity excluded), most commonly control forces and air resistance. The total mass of the UAV is m_c, and $\boldsymbol{I}_b$ is its body-fixed inertia matrix. $\boldsymbol{f}^n$ is the vertical thrust directed along the body z-axis' negative direction decomposed in $\{n\}$ and $\boldsymbol{M}$ is the applied torque from motor to the UAV's body. The gravitational term $\boldsymbol{g}^b$ is defined by $\boldsymbol{R}_b^n(\boldsymbol{\Theta})^T\boldsymbol{g}^n = \boldsymbol{R}_b^n(\boldsymbol{\Theta})^T[0 \quad 0 \quad g]^T$, where g is the gravitational constant. $\boldsymbol{R}_b^n(\boldsymbol{\Theta})$ and $\boldsymbol{T}(\boldsymbol{\Theta})$ are transformation matrices which is defined in Appendix A.

When separated into 4 equations for the four different state types, $\boldsymbol{p}, \boldsymbol{v}, \boldsymbol{\Theta}$ and $\boldsymbol{\omega}$, it leaves

$$\dot{\boldsymbol{p}^n} = \boldsymbol{v}^n \tag{2.5}$$

$$m_c\dot{\boldsymbol{v}}^n = m_c\boldsymbol{g}^n + \boldsymbol{R}(\boldsymbol{\Theta})\boldsymbol{f}^b \tag{2.6}$$

$$\dot{\boldsymbol{\Theta}}^n = \boldsymbol{T}(\boldsymbol{\Theta}^n)\boldsymbol{\omega}^b \tag{2.7}$$

$$\boldsymbol{I}_b\dot{\boldsymbol{\omega}}^b = \boldsymbol{S}(\boldsymbol{I}_b\boldsymbol{\omega}^b)\boldsymbol{\omega}^b + \boldsymbol{M} \tag{2.8}$$

It should be noted that if there is symmetry about all axes as well as that $\boldsymbol{I}_b = c \cdot \boldsymbol{I}_{3\times 3}$ for some c, then $\boldsymbol{S}(\boldsymbol{I}_b\boldsymbol{\omega}^b)\boldsymbol{\omega}^b = \mathbf{0}_{3\times 1}$ as $\boldsymbol{I}_b\boldsymbol{\omega}^b$ and $\boldsymbol{\omega}^b$ are parallel.

2.3 Multicopter Control

If the multicopter are to be able to fly in a controlled manner, an autopilot system has to be created. The following sections will in detail explain the autopilot system of the multicopter.

The most important characteristic of a multicopter control is that it is under-actuated, meaning that it can only afflict influence in a subset of the six degrees of freedom present. As all of the four rotors direct their force downwards, the only translational force aligns with z^b. When it comes to attitude, the four rotors are able to produce torque in all directions because of chosen spin direction of the vehicle (as seen in Figure 2.1), making the attitude control fully actuated. The control of attitude makes it possible to achieve transitional movement by tilting the z^b axis such that $\boldsymbol{f}^b$ decomposes into desired transitional forces.

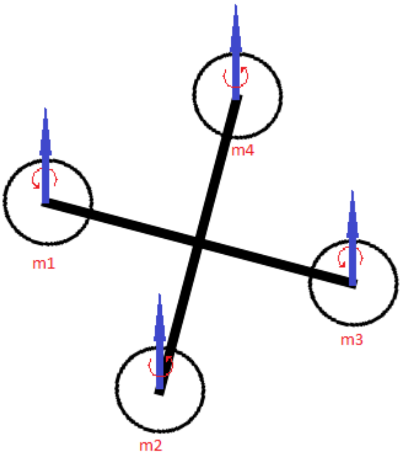

Figure 2.1: Multicopter model with marked rotor directions

In simplified terms, this means that we are restricted by:

$$[1 \;\; 1 \;\; 0] \cdot \dot{\boldsymbol{\nu}}_1^b = 0 \tag{2.9}$$

but as we can control the direction completely, the problem of achieving the correct desired force in $\{n\}$ boils down to finding the correct attitude.

2.4 Equations of motion

The relation between $\boldsymbol{f}^b$ and $\boldsymbol{f}^n$ is described by the following equations:

$$\boldsymbol{f}^n = \boldsymbol{R}_b^n \boldsymbol{f}^b = \boldsymbol{R}_{z,\psi} \boldsymbol{R}_{y,\theta} \boldsymbol{R}_{x,\phi} \begin{bmatrix} 0 \\ 0 \\ -T \end{bmatrix} \tag{2.10}$$

Where T is the sum of motor force in negative z^b. This can be expanded to:

$$f_x^n = -T(\sin\psi \sin\phi + \cos\psi \cos\phi \sin\theta) \tag{2.11}$$

$$f_y^n = -T(\sin\theta \sin\psi \cos\phi - \cos\psi \sin\phi) \tag{2.12}$$

$$f_z^n = -T(\cos\theta \cos\phi) \tag{2.13}$$

However, as the system is able to achieve any f_d^n regardless of heading it is desirable to decouple heading control from roll and pitch. We do this by redefining equation (2.10) as

$$\bar{\boldsymbol{f}} = \boldsymbol{R}_{z,\psi}^T \boldsymbol{f}^n = \boldsymbol{R}_{y,\theta} \boldsymbol{R}_{x,\phi} \begin{bmatrix} 0 \\ 0 \\ -T \end{bmatrix} \tag{2.14}$$

Expanding equation (2.14), it gives

$$\begin{bmatrix} \bar{f}_x \\ \bar{f}_y \\ \bar{f}_z \end{bmatrix} = \begin{bmatrix} \cos\psi & \sin\psi & 0 \\ -\sin\psi & \cos\psi & 0 \\ 0 & 0 & 1 \end{bmatrix} \begin{bmatrix} f_x \\ f_y \\ f_z \end{bmatrix} = \begin{bmatrix} -T\cos\phi\sin\theta \\ -T\sin\phi \\ -T\cos\phi\cos\theta \end{bmatrix} \tag{2.15}$$

2.5 PD controller for transitional movement

As no disturbances are modeled in the environment the multicopter operates in, there is no need for any integral effect on the autopilot's controllers. A PD controller will therefore suffice.

The Equations (2.5)-(2.6) describe the system of transitional movement as a second-order differential equation. The driving forces are gravity and thrust force from the rotors. For simplicity, the term $\boldsymbol{R}(\boldsymbol{\Theta})\boldsymbol{f}^b$ could be redefined as $\boldsymbol{f}^n$, since attitude control allows for any needed $\boldsymbol{R}(\boldsymbol{\Theta})$ giving $\boldsymbol{R}(\boldsymbol{\Theta})\boldsymbol{f}^b = \boldsymbol{f}^n$. The angle allocation to realize this will be discussed later on.

Now to define the controller. The first thing that should be considered is gravity compensation. As the direction and magnitude of the gravitational force is sufficiently accurately known, its easy to cancel it out.
Let the transitional control law be defined by:

$$\boldsymbol{f}^n = -m_c\boldsymbol{g} + \boldsymbol{\alpha}_t \tag{2.16}$$

Where $\boldsymbol{\alpha}_t$ is the PD reference controller for position and velocity. To achieve control over both velocity and position, reference feedforward is needed for them both. It is therefore assumed that the autopilot is provided with $\boldsymbol{p}_d$ and $\boldsymbol{v}_d$ where the reference velocity is defined $\boldsymbol{v}_d = \dot{\boldsymbol{p}}_d$.

Choosing the control law

$$\boldsymbol{\alpha}_t = m_c\dot{\boldsymbol{v}}_d - m_c\boldsymbol{K}_d\tilde{\boldsymbol{v}} - m_c\boldsymbol{K}_p\tilde{\boldsymbol{p}} \tag{2.17}$$

Where $\tilde{\boldsymbol{p}}$ and $\tilde{\boldsymbol{v}}$ is the error in position an velocity, defined as $\boldsymbol{p} - \boldsymbol{p}_d$ and $\boldsymbol{v} - \boldsymbol{v}_d$. Considering $\boldsymbol{a} = \ddot{\boldsymbol{p}}$ and $\boldsymbol{v} = \dot{\boldsymbol{p}}$, This gives the transitional dynamics

$$\ddot{\tilde{\boldsymbol{p}}} + \boldsymbol{K}_d\dot{\tilde{\boldsymbol{p}}} + \boldsymbol{K}_p\tilde{\boldsymbol{p}} = \boldsymbol{0} \tag{2.18}$$

with a globally exponentially stable equilibrium at $(\tilde{\boldsymbol{p}}, \tilde{\boldsymbol{v}}) = (0, 0)$ given $\boldsymbol{K}_d > \boldsymbol{0}$ and $\boldsymbol{K}_p > \boldsymbol{0}$.

2.6 Control allocation

As discussed in Section 2.4, to turn the rotor thrust into the desired force in $\{n\}$, a certain attitude has to be achieved. Heading could be controlled independently of the other two angles and would not affect the span of reachable states. The main focus of the angle allocation algorithm is therefore roll and pitch. To make the algorithm independent of heading, it is based upon the transformed force $\bar{\boldsymbol{f}}$ from equation (2.14).

ALGORITHM 1

1. *Choose the desired thrust, T, which compensates for the current rotation of the system: $T = -\frac{\bar{f}_z}{\cos\phi\cos\theta}$, where ϕ and θ are the current values for the roll and pitch angles.*
2. *Assign the pitch and roll angle that give the desired decomposition, based upon functions derived from the second part of equation* (2.15):

$$\theta_d = \operatorname{atan2}(\bar{f}_x, \bar{f}_z), \quad \phi_d = -\operatorname{atan2}\Big(\bar{f}_y, \sqrt{\bar{f}_x^2 + \bar{f}_z^2}\Big) \tag{2.19}$$

These results for step 1 is easily verified by inspecting the equation $\bar{f}_z = -T\cos\phi\cos\theta$. To make the right hand side equal to $\bar{f}_z$, one must choose T to be equal $-\frac{\bar{f}_z}{\cos\phi\cos\theta}$ The angle allocation is trivial to verify using the same set of equations and inserting for $\bar{f}_x, \bar{f}_y$ and $\bar{f}_z$ and utilizing the trigonometric identity $\sin^2 x + \cos^2 x = 1$.

2.7 PD controller for angular movement

When the desired angles are found from equation (2.19), the reference is used by a PD controller for angular movement. Much like the controller for transitional movement, this controller is based upon the equations of motion, but the angular ones: (2.7)-(2.8). First, we need the control law $\boldsymbol{M}$ to compensate for the rigid-body Coriolis effect $\boldsymbol{S}(\boldsymbol{I}_b\boldsymbol{\omega})\boldsymbol{\omega}$.
Defining the angular control law as:

$$\boldsymbol{M} = -\boldsymbol{S}(\boldsymbol{I}_b\boldsymbol{\omega})\boldsymbol{\omega} + \boldsymbol{\alpha}_r \tag{2.20}$$

Gives the dynamics

$$\boldsymbol{I}_b\dot{\boldsymbol{\omega}} = \boldsymbol{\alpha}_r \tag{2.21}$$

It is now left to choose the dynamics of the angular movement. Choosing the control law:

$$\boldsymbol{\alpha}_r = -\mathbf{K}_d\boldsymbol{\omega} - \boldsymbol{T}^\top\mathbf{K}_p\tilde{\Theta} \tag{2.22}$$

gives us a globally asymptotically stable system for angular movement. Proof of stability could be found in Appendix B.

2.8 Successive loop closure

Considering what has already been shown, the transitional controller is globally exponential stability (GES), while the the rotational controller is just globally asymptotically stable (GAS). The problem is that these two systems are coupled, as shown in figure 2.2, and no stability is showed for the cascaded system. This is where the Successive Loop Closure technique, described in (Beard and McLain, 2012, Chapter 6), is introduced. The concept of this method is to separate the bandwidth of the two different controllers, to the point where the the slower controller sees the faster one as nigh-instant. In this case it would mean that $\boldsymbol{\Theta}_d \approx \boldsymbol{\Theta}$ seen from the transitional controllers point of view, which in turn means that $\boldsymbol{\tau}_d \approx \boldsymbol{\tau}$. This is visualized in Figure 2.3.

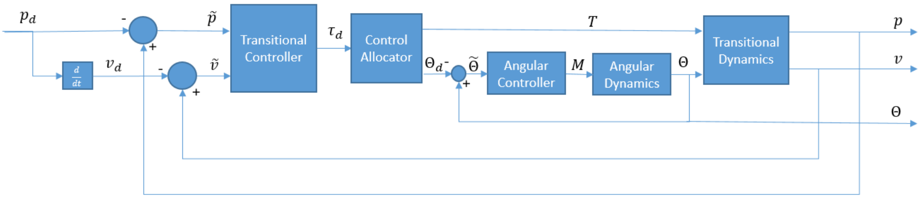

Figure 2.2: Block diagram of autopilot

This method requires the bandwidth of the regulated systems to be controllable, which generally means linear systems and being able to be written on the form:

$$\ddot{x} + 2\zeta\omega_n\dot{x} + \omega_n^2 x = 0 \tag{2.23}$$

where ζ is the dampening factor and ω_n is the natural frequency of the system. This is however not the case for the angular controller, as that is non-linear. Experimental results however support that treating it like it was a linear controller achieves a well behaved controller which is able to follow the reference $\boldsymbol{p}_d$ given proper tuning.

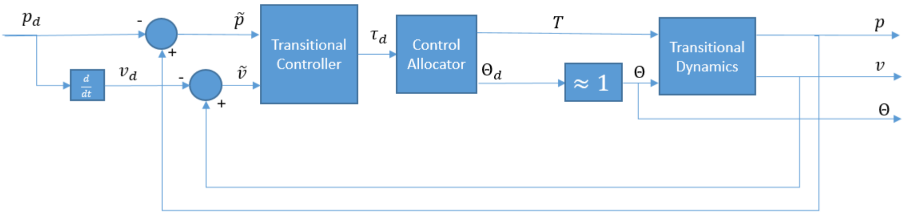

Figure 2.3: Block diagram of autopilot, seen from the transitional controller's perspective

2.9 Speed and thrust saturation

As the simulated system has no limitation to its actuators, it cannot accurately simulate the behaviour of a real system. By imposing conservative restriction on the output of the transitional controller, the system is able to behave realistically. Imposing a simple constraint on $\boldsymbol{\alpha}$

$$\boldsymbol{\alpha} = sat(\boldsymbol{\alpha}, \frac{m_c \cdot g}{n}) \tag{2.24}$$

where *sat* is defined

$$sat(\boldsymbol{x}, a) = \begin{cases} x_i = x_i, & |x_i| < |a| \\ x_i = |a| \cdot sgn(x_i), & |x_i| \geq |a| \end{cases} \tag{2.25}$$

and n is determining the maximum acceleration provided in any direction by the controller.

The speed limitation is imposed as a consequence of the actuator saturation. For the controller to be able to stop without overshooting after it had been accelerating long enough with no speed limitation, it would have to exceed its acceleration limits in the opposite direction. As a result of the actuator saturation, there now exists a maximum speed v_m that is the limit for what the restricted actuators are able to stop without overshooting.
The speed limiter is defined as the following effect on $\boldsymbol{\alpha}$

$$\alpha_i = \begin{cases} sat(\alpha_i, \frac{m_c \cdot g}{n}), & -v_m \leq v_i^n \leq v_m \\ min(sat(\alpha_i, \frac{m_c \cdot g}{n}), 0), & v_m \leq v_i^n \\ max(sat(\alpha_i, \frac{m_c \cdot g}{n}), 0), & -v_m \geq v_i^n \end{cases} \tag{2.26}$$

2.10 Visualization Tool

The tuning of the autopilot's controller parameters had to be redone for this project. The initial simulator were both tuned for and saturated to very low accelerations and velocities. As some of the methods that will be discussed later needed a sufficiently large acceleration vector, this had to change. To make the effect the tuning has on the controller more visible, a tool which could visualize the vehicle during its flight, as well as its flight path, was implemented.

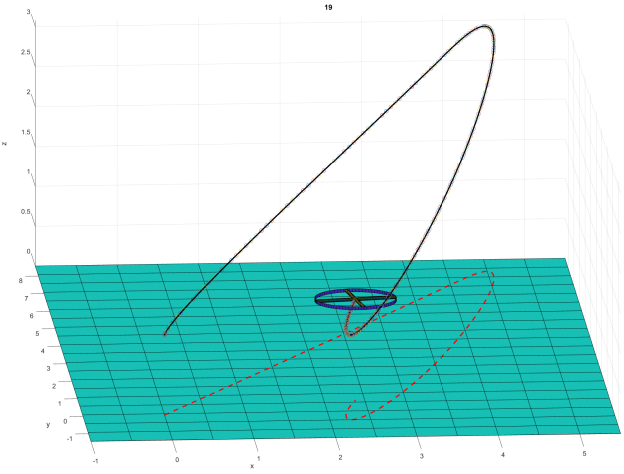

Figure 2.4: 3D-plot showing the multicopter's position, orientation, flight path and 2D-projected path at t=19.

This functionality does not show the flight in simulation time, but is rather as a stand-alone function that only requires log information on $\boldsymbol{p}(t)$ and $\boldsymbol{\Theta}(t)$. The use of the function $\mathit{animatehelicopter}\big(\boldsymbol{p}(t), \boldsymbol{\Theta}(t), t\big)$ will start an animation sequence that shows the multicopter as a minimalistic, rigid body model represented by a cross with a ring encircling the cross. The animation shows the rigid body model's position and orientation, as well as at which time. It also shows the traveled flight path as a black line, as well as its 2D-projected cohering path on the $(x, y, 0)$-plane. The result could be seen in Figure 2.4.

Chapter 3

State Estimation

For a vehicle to be able to move based upon position waypoints, it must first have good estimates of its own position. There are many ways to do this, but the most common are through the use of observers that combine system models with measurements. The one in use for this project would be the direct discrete Kalman filter, which will be covered in Section 3.2.

While this chapter covers the methods necessary for the multicopter to travels reliably between waypoints, additional methods and sensors might be introduced later on as ways to complement and improve the existing, basic navigation methods.

3.1 Sensor models

For the Kalman filter, two different sensor systems are used. To estimate position accurately and continuously, the strap-down accelerometers is the normal choice. To correct and complement the accelerometers, a pseudorange measurement system is used.

3.1.1 Accelerometer model

The accelerometer is used for high-frequent and accurate position estimates, integrating measured acceleration over time to indirectly measure position. The major draw-back of accelerometers in terms of position estimates is that small inaccuracies, so called biases, causes the estimated position to drift over time. The accelerometer model used is found in (Farrell, 2008, Chapter 10.2), and defined

$$\boldsymbol{a}^b_{imu} = \boldsymbol{a}^b - \boldsymbol{g}^b + \boldsymbol{b}^b_a + \boldsymbol{\epsilon}_{imu} \tag{3.1}$$

where $\boldsymbol{a}^b$ is true accelerations, $\boldsymbol{g}^b$ is the gravitational accelerations, $\boldsymbol{b}^b_a$ is the bias components of the accelerometer and $\boldsymbol{\epsilon}_{imu}$ is the Gaussian white noise components
Notice that all the components of the accelerometer measurement are defined in $\{b\}$, as this is a strap-down system. The used IMU frequency is chosen as 100 Hz.

The bias components has both a dynamic and a static component. Its dynamic component is modeled as a Gauss-Markov process, described in (Fossen, 2011, Chapter 8.3). The static component is a stationary value that the Gauss-Markov process is drawn towards.

$$\dot{\boldsymbol{b}}_a = -T_b(\boldsymbol{b}_a - \boldsymbol{b}_{a_s}) - T_b\boldsymbol{w} \tag{3.2}$$

where $\boldsymbol{b}_{a_s}$ is the stationary component, T_b is the time constant of the dynamics and $\boldsymbol{w}$ is the Gaussian white noise driving the Gauss-Markov process.

3.1.2 Pseudorange measurement model

For correcting the estimation of position due to accelerometer biases, a position aiding measurement system is needed. As the method for position aiding is not relevant, so a pseudorange measurement system is used. The most typical pseudorange measurement system today is GNSS. While these systems have the advantage of in general being globally available, it is unreliable for indoor usage because of attenuation and indoor multipathing. The substitute system used indoor would therefore be a set of radio transmitting beacons. Theoretically, this would be an identical case to the use of GNSS, as the radio transponders mimics satellites, but still has the advantage of having a chosen and stationary position. The measurement model for pseudorange is found in (Johansen and Fossen, 2016) and defined

$$y_i = \left\|\boldsymbol{p} - \boldsymbol{p}_i\right\|_2 + \beta + \epsilon_i \tag{3.3}$$

Where y_i is the measured value from transponder i, $\boldsymbol{p}$ is the position of the reciever, $\boldsymbol{p}_i$ is the position of transponder i, β is the reciever clock error and ϵ_i is the noice affecting measurement i. However, for sake of simplicity, a perfectly tuned clock will be assumed, eliminating β from the equation.

Assumption 2: The receiver clock bias is absent for our system: $\beta = 0$, giving the sensor model:

$$y_i = \left\|\boldsymbol{p} - \boldsymbol{p}_i\right\|_2 + \epsilon_i \tag{3.4}$$

The pseudorange measurements has the disadvantage of being at a much slower measurement rate than the accelerometer. To simulate this the measurement rate of the pseudorange system is chosen as 10 Hz.

3.2 Discrete Kalman filtration

The Kalman filter is an optimal observer for linear systems with respect to error variance, given priori knowledge of the unmodeled uncertainties, represented by noise, of both the model process and the sensor measurements. The process uses an initial gaussian estimate, described by the mean of the gaussian distributions $\hat{x}_0^-$ and its error covariance matrix $\boldsymbol{P}_0^-$, defined by $\boldsymbol{P}_k = \mathrm{E}[(\boldsymbol{x}_k - \hat{\boldsymbol{x}}_k)(\boldsymbol{x}_k - \hat{\boldsymbol{x}}_k)^T]$. It then constantly corrects with measurement information and predicts ahead with the model.

3.2.1 Properties of the Kalman filter

According to (Vik, 2014), the following assumptions are made about the Kalman filter:

- *The process noise and measurement noise are white and Gaussian.*

- *The initial probability distribution of the states are Gaussian.*
- *The system is linear.*
- *The system is observable.*

If all these requirements are met, the Kalman filter has the following properties:

- *The estimate is unbiased and minimum variance.*
- *The Kalman filter is the optimal (linear or nonlinear) state estimator*
- *The Kalman filter is asymptotically stable*

The requirements for the Kalman filter will be discussed for the system in use later, as they are important to understand the performance of the estimator.

3.2.2 Linear Kalman filter

The discrete linear Kalman filter assumes a linear process described by the normal state space equations

$$\boldsymbol{x}_{k+1} = \boldsymbol{A}_k \boldsymbol{x}_k + \boldsymbol{B}_k \boldsymbol{u}_k + \boldsymbol{w}_k \tag{3.5}$$

$$\boldsymbol{y}_k = \boldsymbol{H}_k \boldsymbol{x}_k + \boldsymbol{v}_k \tag{3.6}$$

where $\boldsymbol{x}_k \in \mathbb{R}^n$ is the states at $t = k$, $\boldsymbol{u}_k \in \mathbb{R}^p$ is the input to the system at $t = k$, $\boldsymbol{y}_k \in \mathbb{R}^m$ is the measurements at $t = k$, $\boldsymbol{w}_k \in \mathbb{R}^n$ is unmodeled process uncertainties and $\boldsymbol{v}_k \in \mathbb{R}^n$ is unmodeled measurement uncertainties. Both of the uncertainties are modeled by Gaussian white noise that are uncorrelated to anything else that itself at the same time step.
The flow of a Linear Kalman filter is described by Figure 3.1.

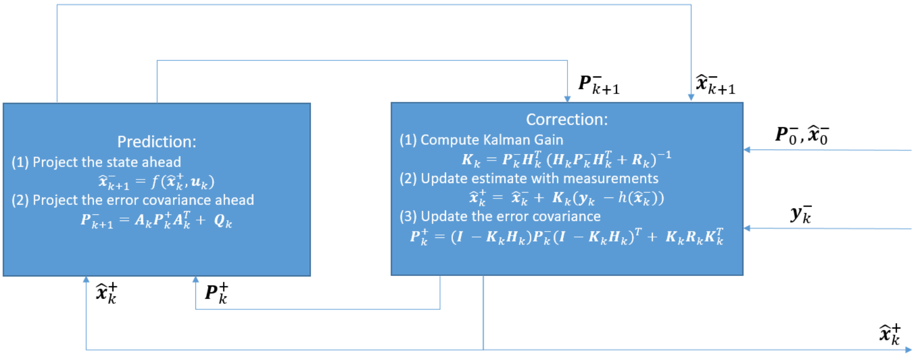

Figure 3.1: Block diagram of information flow in a Linear Kalman filter

The equations of a linear Kalman filter are as follows:

Correction:

$$\boldsymbol{K}_k = \boldsymbol{P}_k^{-} \boldsymbol{H}_k^T (\boldsymbol{H}_k \boldsymbol{P}_k^{-} \boldsymbol{H}_k^T + \boldsymbol{R}_k)^{-1} \tag{3.7}$$

$$\hat{\boldsymbol{x}}_k^{+} = \hat{\boldsymbol{x}}_k^{-} + \boldsymbol{K}_k (\boldsymbol{y}_k - \boldsymbol{H}_k \hat{\boldsymbol{x}}_k^{-}) \tag{3.8}$$

$$\begin{aligned} \boldsymbol{P}_k^{+} &= (\boldsymbol{I}_n - \boldsymbol{K}_k \boldsymbol{H}_k) \boldsymbol{P}_k^{-} (\boldsymbol{I}_n - \boldsymbol{K}_k \boldsymbol{H}_k)^T \\ &\quad + \boldsymbol{K}_k \boldsymbol{R}_k \boldsymbol{K}_k^T \end{aligned} \tag{3.9}$$

Prediction:

$$\hat{\boldsymbol{x}}_{k+1}^{-} = \boldsymbol{A}_k \hat{\boldsymbol{x}}_k^{+} + \boldsymbol{B}_k \boldsymbol{u}_k \tag{3.10}$$

$$\boldsymbol{P}_{k+1}^{-} = \boldsymbol{A}_k \boldsymbol{P}_k^{+} \boldsymbol{A}_k^T + \boldsymbol{Q}_k \tag{3.11}$$

where $\boldsymbol{R}_k = E[\boldsymbol{v}_k \boldsymbol{v}_k^T] \in \mathbb{R}^{m \times m}$, $\boldsymbol{Q}_k = E[\boldsymbol{w}_k \boldsymbol{w}_k^T] \in \mathbb{R}^{n \times n}$ and $\boldsymbol{K}_k \in \mathbb{R}^{n \times m}$ is the gain that decides the weighting between model and measurement.

Explained shortly, the two steps of the Kalman filter consists of having a previous state estimate, $\hat{\boldsymbol{x}}_k^{-}$, with an uncertainty dictated by the error covariance matrix $\boldsymbol{P}_k^{-}$. Based on the different system parameters, error uncertainty and measurement uncertainty, a weighting is given for how much the new measurements are trusted. The filtration is then done, and new state estimates are given, with a new uncertainty less than or equal to the unfiltered one. The final part is to use the model to predict ahead a new unfiltered state for the next step of filtration.

The output of the filter would be the filtered state with or without its probability distribution.

3.2.3 Extended Kalman Filter

Most real life systems are not linear. The general, nonlinear form of a state space dynamics should therefore be used.

A problem arises when the process no longer is linear. When a normal distribution is put through a nonlinear system, the output is in general no longer normally distributed.

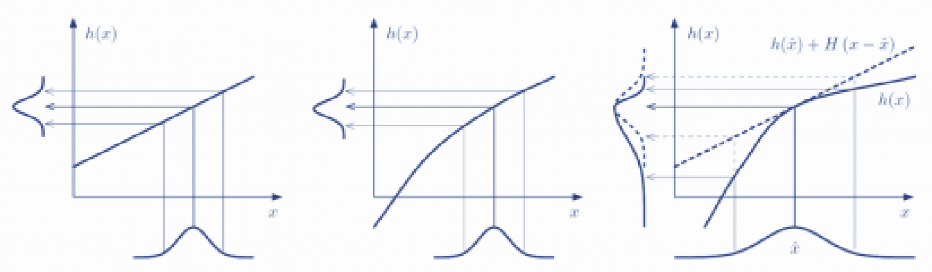

Figure 3.2: Illustration of a normal distribution through a linear system, a near-linear system and a linearization of the nonlinear system.
Source: (Baltzer, 2013)

As can be seen in the rightmost illustration of figure 3.2, the real transformation of a normal distribution through a nonlinear function is no longer normal. To keep the distribution Gaussian, the Extended Kalman filter linearize the nonlinear system functions around the current mean of the estimated state.
The updated flow chart is then:

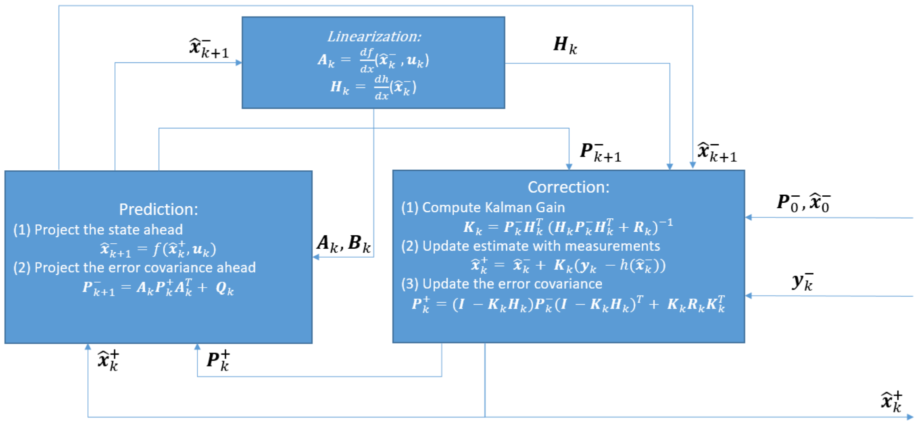

Figure 3.3: Block diagram of information flow in an Extended Kalman filter

And the new equations will be:

Linearization:

$$\boldsymbol{A}_k = \left.\frac{df(\boldsymbol{x}, \boldsymbol{u})}{d\boldsymbol{x}}\right|_{\boldsymbol{x}=\hat{\boldsymbol{x}}_k^-, \boldsymbol{u}=\boldsymbol{u}_k} \tag{3.12a}$$

$$\boldsymbol{H}_k = \left.\frac{dh(\boldsymbol{x})}{d\boldsymbol{x}}\right|_{\boldsymbol{x}=\hat{\boldsymbol{x}}_k^-} \tag{3.12b}$$

Correction:

$$\boldsymbol{K}_k = \boldsymbol{P}_k^- \boldsymbol{H}_k^T (\boldsymbol{H}_k \boldsymbol{P}_k^- \boldsymbol{H}_k^T + \boldsymbol{R}_k)^{-1} \tag{3.12c}$$

$$\hat{\boldsymbol{x}}_k^+ = \hat{\boldsymbol{x}}_k^- + \boldsymbol{K}_k(\boldsymbol{y}_k - h(\hat{\boldsymbol{x}}_k^-)) \tag{3.12d}$$

$$\begin{aligned}\boldsymbol{P}_k^+ &= (\boldsymbol{I}_n - \boldsymbol{K}_k \boldsymbol{H}_k) \boldsymbol{P}_k^- (\boldsymbol{I}_n - \boldsymbol{K}_k \boldsymbol{H}_k)^T \\ &\quad + \boldsymbol{K}_k \boldsymbol{R}_k \boldsymbol{K}_k^T\end{aligned} \tag{3.12e}$$

Prediction:

$$\hat{\boldsymbol{x}}_{k+1}^- = f(\hat{\boldsymbol{x}}_k^+, \boldsymbol{u}_k) \tag{3.12f}$$

$$\boldsymbol{P}_{k+1}^- = \boldsymbol{A}_k \boldsymbol{P}_k^+ \boldsymbol{A}_k^T + \boldsymbol{Q}_k \tag{3.12g}$$

Notice that the transformation of the estimated mean is done with the nonlinear function, while the error covariance distribution is done with the linearized matrix. The same holds true for the innovation term, Equation (3.12d) where the real observation function is used, while the linearized version is used everywhere else.

As the Extended Kalman filter breaks the linearity assumption about the Kalman filter, it can no longer guarantee optimallity. However, as the error caused by linearization is dependent on how nonlinear the function is as well as the distance from the point linearized about, we can assume near-optimal performance as long as the following is fulfilled:

- The process function f and the measurement function h are locally linear
- The variance of the uncertainty is sufficiently small s.t. the probability density function is mostly contained within the are where the error of the linearized model is negligible.

3.3 Multicopter's Kalman filter

The system simulated is thoroughly described in Chapter 2, so what remains is to implement a Kalman filter observer for state estimation. To limit the scope of the state estimation, it will at first be assumed that the attitude is known. The focus will therefore be on position estimation, something that greatly limits the number of states in the Kalman filter. As the Kalman filter operates in $\{n\}$, the state space model is a simplified version of Equation (2.5) and (2.6), just that the gravitational and thrust forces is combined into the compensated accelerometer measurements, that will act like input for the system. The system is also augmented with bias states to estimate the accelerometer biases.

$$\begin{bmatrix} \dot{\hat{\boldsymbol{p}}}^n \\ \dot{\hat{\boldsymbol{v}}}^n \\ \dot{\hat{\boldsymbol{b}}}^n \end{bmatrix} = \begin{bmatrix} \mathbf{0}_{3\times3} & \boldsymbol{I}_3 & \mathbf{0}_{3\times3} \\ \mathbf{0}_{3\times3} & \mathbf{0}_{3\times3} & -\boldsymbol{I}_3 \\ \mathbf{0}_{3\times3} & \mathbf{0}_{3\times3} & \mathbf{0}_{3\times3} \end{bmatrix} \begin{bmatrix} \hat{\boldsymbol{p}}^n \\ \hat{\boldsymbol{v}}^n \\ \hat{\boldsymbol{b}}^n \end{bmatrix} + \begin{bmatrix} \mathbf{0}_{3\times3} \\ \boldsymbol{I}_{3\times3} \\ \mathbf{0}_{3\times3} \end{bmatrix} \hat{\boldsymbol{a}}^n \tag{3.13}$$

Where $\hat{\boldsymbol{b}}^n$ is the estimated accelerometer biases in $\{n\}$ and $\hat{\boldsymbol{a}}^n = \boldsymbol{R}(\boldsymbol{\Theta})\boldsymbol{a}^b_{IMU} - \boldsymbol{g}^n$.

System used in a discrete Kalman filter has to be discretized. The discretization equation could be found at (Fossen, 2011, Chapter 11.3) and are the following:

$$\boldsymbol{A}_d = e^{\boldsymbol{A}h} \text{ giving } \boldsymbol{A}_d = \begin{bmatrix} \boldsymbol{I}_3 & h\boldsymbol{I}_3 & -\frac{h^2}{2}\boldsymbol{I}_2 \\ \mathbf{0}_{3\times3} & \boldsymbol{I}_3 & -h\boldsymbol{I}_3 \\ \mathbf{0}_{3\times3} & \mathbf{0}_{3\times3} & \boldsymbol{I}_3 \end{bmatrix} \tag{3.14}$$

$$\boldsymbol{B}_d = \boldsymbol{A}^{-1}(e^{\boldsymbol{A}h} - \boldsymbol{I}_n)\boldsymbol{B} \tag{3.15}$$

However, as the $\boldsymbol{A}$ matrix in use is singular, Equation (3.15) is not well behaved. To avoid this problem, an alternative formulation of this equation could be achieved through algebraic manipulation. (Balchen et al., 2003, Chapter 3.3) gives the alternative formulation:

$$\boldsymbol{B}_d = h\sum_{n=0}^{\infty}\frac{1}{(n+1)!}(\boldsymbol{A}h)^n\boldsymbol{B} = \begin{bmatrix}\frac{h^2}{2}\boldsymbol{I}_3\\ h\boldsymbol{I}_3\\ \boldsymbol{0}_{3\times3}\end{bmatrix} \tag{3.16}$$

The other part of the state space model, the measurement equation has to be modeled. Equation (3.4), states that the pseudorange measurements are defined by the geometric distance from the transponder to the receiver. This makes

$$\boldsymbol{y} = h(\boldsymbol{x}) = \begin{bmatrix}||\boldsymbol{p}-\boldsymbol{p}_1||_2+\boldsymbol{\epsilon}_1\\ ||\boldsymbol{p}-\boldsymbol{p}_2||_2+\boldsymbol{\epsilon}_2\\ \vdots\\ ||\boldsymbol{p}-\boldsymbol{p}_m||_2+\boldsymbol{\epsilon}_m\end{bmatrix} \tag{3.17}$$

As the measurement function is a nonlinear function, linearization is needed to make use of the Kalman filter for nonlinear systems. Linearization of $h(\boldsymbol{x})$ with respect to $\boldsymbol{x}$ gives

$$\boldsymbol{H} = \frac{df}{d\boldsymbol{x}}(\boldsymbol{x}) = \begin{bmatrix}\breve{\boldsymbol{p}}_1^T & \boldsymbol{0}_{1\times3} & \boldsymbol{0}_{1\times3}\\ \breve{\boldsymbol{p}}_2^T & \boldsymbol{0}_{1\times3} & \boldsymbol{0}_{1\times3}\\ \vdots & \vdots & \vdots\\ \breve{\boldsymbol{p}}_m^T & \boldsymbol{0}_{1\times3} & \boldsymbol{0}_{1\times3}\end{bmatrix} \tag{3.18}$$

where $\breve{\boldsymbol{p}}_i = \begin{bmatrix}\frac{x-x_i}{||\boldsymbol{p}-\boldsymbol{p}_i||_2}, & \frac{y-y_i}{||\boldsymbol{p}-\boldsymbol{p}_i||_2}, & \frac{z-z_i}{||\boldsymbol{p}-\boldsymbol{p}_i||_2}\end{bmatrix}^T$
As can be seen, the system's nonlinear measurement equation demands for the use of an extended Kalman filter.

The system is now able to produce position estimates. This means that the autopilot now is able to regulate its position to some reference, assuming the angle is known. The information flow of the entire navigation scheme is illustrated in Figure 3.4

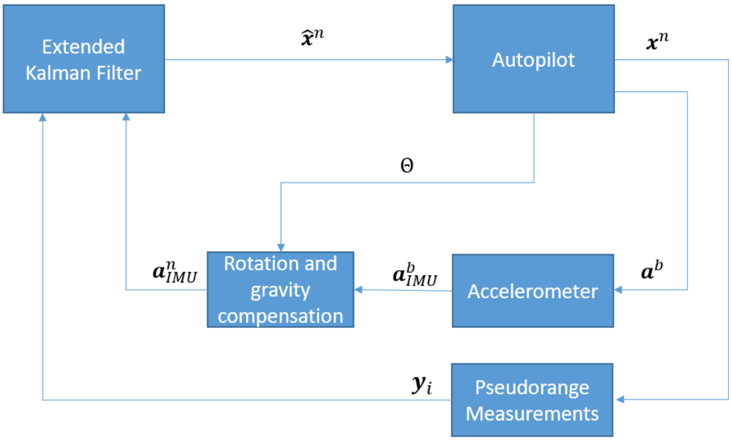

Figure 3.4: Information flow of the system

3.3.1 Observability of system

As mentioned in Section 3.2.1 one of the requirements for the states of a Kalman filter to converge is that system is observable. To show that the system is observable, the observability gramian must be shown to be non-singular. This result of the observation analysis is confirmed by the work done in (Johansen et al., 2017), which greatly contributed to the last steps.

$$
\begin{aligned}
\boldsymbol{W}_0 &= \int_{t_0}^{t_0+T} (\boldsymbol{H}e^{\boldsymbol{A}\tau})^T(\boldsymbol{H}e^{\boldsymbol{A}\tau})d\tau \\
&= \int_{t_0}^{t_0+T} \left(\begin{bmatrix} \breve{\boldsymbol{p}}_1^T & \boldsymbol{0}_{1\times3} & \boldsymbol{0}_{1\times3} \\ \breve{\boldsymbol{p}}_2^T & \boldsymbol{0}_{1\times3} & \boldsymbol{0}_{1\times3} \\ \vdots & \vdots & \vdots \\ \breve{\boldsymbol{p}}_m^T & \boldsymbol{0}_{1\times3} & \boldsymbol{0}_{1\times3} \end{bmatrix} \begin{bmatrix} \boldsymbol{I}_3 & \tau\boldsymbol{I}_3 & -\frac{\tau^2}{2}\boldsymbol{I}_2 \\ \boldsymbol{0}_{3\times3} & \boldsymbol{I}_3 & -\tau\boldsymbol{I}_3 \\ \boldsymbol{0}_{3\times3} & \boldsymbol{0}_{3\times3} & \boldsymbol{I}_3 \end{bmatrix} \right)^T \\
&\quad \left(\begin{bmatrix} \breve{\boldsymbol{p}}_1^T & \boldsymbol{0}_{1\times3} & \boldsymbol{0}_{1\times3} \\ \breve{\boldsymbol{p}}_2^T & \boldsymbol{0}_{1\times3} & \boldsymbol{0}_{1\times3} \\ \vdots & \vdots & \vdots \\ \breve{\boldsymbol{p}}_m^T & \boldsymbol{0}_{1\times3} & \boldsymbol{0}_{1\times3} \end{bmatrix} \begin{bmatrix} \boldsymbol{I}_3 & \tau\boldsymbol{I}_3 & -\frac{\tau^2}{2}\boldsymbol{I}_2 \\ \boldsymbol{0}_{3\times3} & \boldsymbol{I}_3 & -\tau\boldsymbol{I}_3 \\ \boldsymbol{0}_{3\times3} & \boldsymbol{0}_{3\times3} & \boldsymbol{I}_3 \end{bmatrix} \right) d\tau \\
&= \int_{t_0}^{t_0+T} \begin{bmatrix} \breve{\boldsymbol{p}}_1^T & \tau\breve{\boldsymbol{p}}_1^T & -\frac{\tau^2}{2}\breve{\boldsymbol{p}}_1^T \\ \breve{\boldsymbol{p}}_2^T & \tau\breve{\boldsymbol{p}}_2^T & -\frac{\tau^2}{2}\breve{\boldsymbol{p}}_2^T \\ \vdots & \vdots & \vdots \\ \breve{\boldsymbol{p}}_m^T & \tau\breve{\boldsymbol{p}}_m^T & -\frac{\tau^2}{2}\breve{\boldsymbol{p}}_m^T \end{bmatrix}^T \begin{bmatrix} \breve{\boldsymbol{p}}_1^T & \tau\breve{\boldsymbol{p}}_1^T & -\frac{\tau^2}{2}\breve{\boldsymbol{p}}_1^T \\ \breve{\boldsymbol{p}}_2^T & \tau\breve{\boldsymbol{p}}_2^T & -\frac{\tau^2}{2}\breve{\boldsymbol{p}}_2^T \\ \vdots & \vdots & \vdots \\ \breve{\boldsymbol{p}}_m^T & \tau\breve{\boldsymbol{p}}_m^T & -\frac{\tau^2}{2}\breve{\boldsymbol{p}}_m^T \end{bmatrix} d\tau \\
&\quad \int_{t_0}^{t_0+T} \begin{bmatrix} \bar{\boldsymbol{P}} & \tau\bar{\boldsymbol{P}} & -\frac{\tau^2}{2}\bar{\boldsymbol{P}} \\ \tau\bar{\boldsymbol{P}} & \tau^2\bar{\boldsymbol{P}} & -\frac{\tau^3}{2}\bar{\boldsymbol{P}} \\ -\frac{\tau^2}{2}\bar{\boldsymbol{P}} & -\frac{\tau^3}{2}\bar{\boldsymbol{P}} & \frac{\tau^4}{4}\bar{\boldsymbol{P}} \end{bmatrix} d\tau
\end{aligned}
$$

where $\bar{\boldsymbol{P}} = \sum_{n=1}^{m} \breve{\boldsymbol{p}}_n\breve{\boldsymbol{p}}_n^T$. This in turn gives observability gramian:

$$
\boldsymbol{W}_0 = \int_{t_0}^{t_0+T} \underbrace{\begin{bmatrix} 1 & \tau & -\frac{\tau^2}{2} \\ \tau & \tau^2 & -\frac{\tau^3}{2} \\ -\frac{\tau^2}{2} & -\frac{\tau^3}{2} & \frac{\tau^4}{4} \end{bmatrix}}_{\boldsymbol{G}(\tau)} \otimes \bar{\boldsymbol{P}} \; d\tau \tag{3.19}
$$

If it could be shown that both $\boldsymbol{G}(\tau)$ and $\bar{\boldsymbol{P}}$ have full rank, the observability gramian will be non-singular, which implies observability of the system. Using the proof shown in Appendix C, its given that $\bar{\boldsymbol{P}}$ has full rank if the vectors from the pseudorange receiver to the transponders spans at least a three-dimensional space. Showing that $\int_{t_0}^{t_0+T} \boldsymbol{G}(\tau)d\tau$ has full rank could be done by inspecting

$$
\int_{t_0}^{t_0+T} \begin{bmatrix} 1 & \tau & -\frac{\tau^2}{2} \\ \tau & \tau^2 & -\frac{\tau^3}{2} \\ -\frac{\tau^2}{2} & -\frac{\tau^3}{2} & \frac{\tau^4}{4} \end{bmatrix} d\tau = \begin{bmatrix} \tau & \frac{\tau^2}{2} & -\frac{\tau^3}{6} \\ \frac{\tau^2}{2} & \frac{\tau^3}{3} & -\frac{\tau^4}{8} \\ -\frac{\tau^3}{6} & -\frac{\tau^4}{8} & \frac{\tau^5}{20} \end{bmatrix} \tag{3.20}
$$

This matrix has full rank, which means that $Rank(\boldsymbol{W}_0) = 3 \times 3 = 9$. As the rank of the observability gramian is equal to the number of states in the Kalman filter, the system is therefore observable.

Chapter 4

Methods

Use of inertial navigation relies on measuring acceleration with accelerometers and angle rates with gyroscopes. The use of integration of acceleration and angular velocity to find position and attitude causes large errors over time as smaller measurement errors accumulates. It is therefore crucial that navigation systems that operates over longer periods of time makes use of complementing methods that are able to correct for errors in position/angle estimates, and possibly even estimate the measurement biases of the IMU. For the translational states, PVA, a GNSS system is the standard choice for a position aiding sensor, giving full PVA-observability given sufficient satellite geometry enough visible satellites.

The story is however quite different when considering the rotational states. To measure the different rotational states, roll pitch and heading, the measurements have to rely on a vector that is not parallel with their axes of rotation. The standard way of measuring roll and pitch will therefore be to use the gravitation vector $\boldsymbol{g}$, which has components along the $\boldsymbol{z}^n$ vector, making it perpendicular to the axes of both roll and pitch. The case is much harder when trying to find a reliable vector to measure the heading angle. Such a vector has to have a measurable vector in the xy-plane that can reliably be measured at any time and position at the globe with the sensory packages available to the multicopter. The remaining viable options for heading estimation all require a specific maneuver to be executed. The dynamics of the multicopter and its velocity constraints, or rather lack of, leaves only one option to use for heading estimation: To compare body-aligned acceleration measurements from the accelerometers to a NED-aligned acceleration estimate observed from the position aiding measurement system. The reason for this will be discussed in Section 4.3.1.

From here and out, it is considered that the system has access to measurements from a strap-down IMU with both accelerometers and gyros. These are of such quality that the system dynamics could be tracked accurately over short periods of time.

4.1 Error in estimation of attitude

The process of finding the transformation between two systems, system $\{a\}$ and system $\{b\}$, will involve measuring the same vector, $\boldsymbol{x}$, decomposed in both systems. This gives two measurements, accompanied by two different measurement errors, that will propagate to the estimate of the angle. (Gade, 2016) provides a relation between the measurement errors and the error in the final angle estimate, which will be shown through an example:

Lets define the vector $\boldsymbol{v}$ as a vector with a non-zero component in the horizontal plane of system $\{a\}$:

$$||\boldsymbol{v} \times \boldsymbol{z}|| = ||\boldsymbol{x}_{horizontal}|| > 0 \tag{4.1}$$

Where $\boldsymbol{z}$ is the unit vector along the z-axis of system $\{a\}$ and $\boldsymbol{v}_{horizontal}$ is the vector corresponding to the horizontal components of vector $\boldsymbol{v}$.

Lets also assume that there are available two different methods of measuring this vector in both system $\{a\}$ and system $\{b\}$, such that:

$$\begin{aligned} \hat{\boldsymbol{v}}^a &= \boldsymbol{v}^a + \delta\boldsymbol{v}^a \\ \hat{\boldsymbol{v}}^b &= \boldsymbol{v}^b + \delta\boldsymbol{v}^b \end{aligned} \tag{4.2}$$

Where $\hat{\boldsymbol{v}}$ is the measured estimate and $\delta\boldsymbol{v}$ represents the estimates deviation from the true vector, $\boldsymbol{v}$

While the $\delta\boldsymbol{v}$ component of both measurements represent the error between the measurement and the true vector, only the parts of the error that are both normal to $\boldsymbol{v}$ and in the horizontal plane of system $\{a\}$ contribute to the final angle estimate error. This might be more easy to understand when considering that error components aligned with the axis of rotation (z-axis) is unaffected by the rotation, and therefore contains no contributing information about it. In addition, components aligned with the measured vector's horizontal component will not change its direction projected on the horizontal plane.

In order to keep the notation as clean easy as possible, the operator $(\delta\boldsymbol{v})_{contr}$ will mean extracting the length of the contributing component by this method:

$$(\delta\boldsymbol{v})_{contr} = \left|\frac{\boldsymbol{v}\times\boldsymbol{z}}{||\boldsymbol{v}||}\cdot\delta\boldsymbol{v}\right| \tag{4.3}$$

Which basically gives the length of the error vector projected along the direction normal to both the z-axis(gives components in horizontal plane) and the vector $\boldsymbol{v}$. Keep in mind that this is the contributing errors when measuring a rotation around $\boldsymbol{z}$ through the vector $\boldsymbol{v}$. If the process involves another simple rotation or another measured vector, the operator extracting contributing components will do likewise.

With that operator in place, the relation between the standard deviation of measurement errors and the standard deviation of the resulting heading error will make sense. This relation assumes uncorrelated measurement errors from the different measurement methods, and comes from a first order approximation:

$$\sigma(\delta\psi) \approx \frac{\sqrt{\sigma\Big((\delta\boldsymbol{v}^a)_{contr}\Big)^2 + \sigma\Big((\delta\boldsymbol{v}^b)_{contr}\Big)^2}}{||\boldsymbol{v}_{horizontal}||} \tag{4.4}$$

Where the σ operator gives the standard deviation of its input.

There is two things about this equation worth a remark. As the relationship between the vector orientations and the angle between them is non-linear, the approximation given be (4.4) is only accurate at errors close to zero. Secondly, inspecting the denominator of the equation shows that errors will be suppressed by a larger measurement vector. Considering this it is clear that a sufficiently large measurement vector is crucial to suppress measurement noise.

4.2 Roll and Pitch Correction Methods

The estimation principle for finding roll and pitch angles are based upon simple mathematics. If a vector is measured which is known to only have components along $\boldsymbol{z}$, but is measured in the body-aligned frame, the relation between the known vectors in the two frames gives an unambiguous measure of the rotations around the x-axis and y-axis. A vector along $\boldsymbol{z}$ that is always in effect on Earth is the gravitational acceleration, $\boldsymbol{g}$. The gravitational component of the acceleration will always be perpendicular to the linearized plane of the NED-frame. With this in mind, the use of the equation:

$$\begin{bmatrix} g_x \\ g_y \\ g_z \end{bmatrix}^b = -\boldsymbol{R}_b^n(\boldsymbol{\Theta}) \begin{bmatrix} 0 \\ 0 \\ g \end{bmatrix}^n = \begin{bmatrix} g\sin(\theta) \\ -g\cos(\theta)\sin(\phi) \\ -g\cos(\theta)\cos(\phi) \end{bmatrix} \tag{4.5}$$

gives the relationship

$$\phi = \tan^{-1}\left(\frac{g_y}{g_z}\right), \qquad \theta = -\tan^{-1}\left(\frac{g_x}{\sqrt{g_y^2 + g_z^2}}\right) \tag{4.6}$$

As the inverse tangent functions only has a range of $(-\frac{\pi}{2}, \frac{\pi}{2})$ and their argument are neatly partitioned into fractions, it might be strange that the *atan2*-function is not used. With a closer look on the equation giving the θ-angle, it is clear that the denominator does not carry information about its direction, being the length of the gravitational vector in the body yz-plane. Using *atan2* on it can therefore only provide angles of three quadrants, without finding the direction of the vector $g_y + g_z$. However, as the assumptions made upon our system gives that $\phi, \theta \in [-\frac{\pi}{2}, \frac{\pi}{2}]$, meaning that it would suffice to use the standard inverse tangent function.

To perform an estimation of roll and pitch by measuring the gravitation vector one only have to measure it in body system. The (plumb bob) gravity vector (i.e the effect of gravitation plus the negligible centripetal acceleration due to the Earth's rotation) is both constant in the same geographical area and very close to vertical in NED. This means that a one-time static precision measurement of the vector in NED would eliminate almost all error contributed for the measurements of gravity in NED.

This leaves the measurement of the gravity vector in body. The simplest way of performing such a measurement is to go back to (3.1), which describes the measurement model for the accelerometer. From the model it can be seen that when the multicopter is at rest ($\boldsymbol{v} = 0 \Rightarrow \boldsymbol{a} = 0$) and the accelerometer biases are estimated, the remaining components of the accelerometer model are:

$$\boldsymbol{a^b}_{imu} \approx -\boldsymbol{g}^b + \boldsymbol{\epsilon}_{imu} \tag{4.7}$$

Leaving only gravity vector and measurement noise.

It is now time to consider under which circumstances the requirements for acceleration is fulfilled, taken into consideration the platform the IMU is mounted on. The only way to avoid $||\boldsymbol{a}|| > 0$ is for the roll and pitch angles to stay at zero.

Any other orientation will result in either a non-zero vertical acceleration by forfeiting gravity compensating lift, or a non-zero rotor thrust that is decomposed into horizontal acceleration. This means that this method for measuring roll and pitch is only accurate when the angles are small, making $\boldsymbol{g} >> \boldsymbol{a}$ and thus let the length of the measured vector suppress the error (following Equation (4.4)). For this reason. This method is best used for online calibration of a system using inertial navigation, making the system able to estimate biases in the gyroscope, and correct for drift in the attitude estimates.

4.3 Heading Measurement

Estimating the heading is a more problematic issue than roll and pitch. The same reason for that the gravitational vector is an ideal vector for measuring roll and pitch, it is equally unfitted for measuring heading. As it run in a direction almost parallel to the heading axis of rotation, any error in the measurement of the $\boldsymbol{g}$-vector will lead to large errors in heading, due to its very small horizontal component.

4.3.1 Possible horizontal vectors

Searching for other vector candidates that both have a significant horizontal component and are measurable in both NED and body, it sums up to (according to (Gade, 2016)) seven different vectors. The utilization feasibility of each vector is highly dependent on the sensor package available to the vehicle, as well as vehicle dynamics. To justify the resulting methods focuses on movement, every fundamental method will be presented and discussed. From now, every fundamental heading estimating method will be referred to as "*Method x*"

Method 1: The magnetic vector field of the Earth (Magnetometer)

A magnetometer, used to measure magnetic fields, are today both low-cost, lightweight, small and self-contained. However, this method suffers from that the Earth's magnetic vector field is not too stable, neither in time or geographically, in addition to that it is ideally pointing towards the magnetic north, instead of the True North (Earth's axis of rotation). This method also faces the problem that a magnetometer is highly susceptible to electromagnetic (EM) noise from the vehicles own magnetic sources, both passive and active. This is not something that could be shielded against either, as the wanted magnetic vector would be equally dampened. The final issue with using the magnetometer is that the magnetic vector field becomes increasingly perpendicular to the Earth's surface at higher latitudes, decreasing the usable horizontal component of the vector. This method is not usable as a main heading sensor on a multicopter due to lack of electromagnetic compatibility. Being driven by electric engines, they produce enough EM-noise to cause unacceptable inaccuracies. If the multicopter were to operate indoor as well, it could also be affected by varying permeability caused by ferromagnetic materials in the surroundings.

Method 2: The angular velocity of the Earth (Gyrocompass)

Using the angular velocity of the Earth is quite similar to using the gravitational vector, as its direction (given known geographical placement) is very accurately known in NED-frame. It uses a combination of gyroscopes to measure the sum of angular rotations from both the Earth and the vehicle ($\boldsymbol{\omega}_{IB}^{b} = \boldsymbol{\omega}_{IE}^{b} + \boldsymbol{\omega}_{EB}^{b}$), and change in the gravity vector or knowledge of a stationary case to give information of the isolated vehicle's angular rotation ($\boldsymbol{\omega}_{EB}^{b}$). Isolating the Earth's rotation in body-frame, it could be compared to the rotation in NED-frame to give heading.

The main advantages of this method is finding the True North, it being self-contained and that it is robust to EM-radiation. On the downside it has a need for gyros with high accuracy, which is significantly more expensive than MEMS-gyros. It also suffers from the same problem as Method 1, in that at large latitudes the Earths rotational axis is parallel to the heading axis of rotation.

Method 3: Vector between external objects: (Star Tracking)

The principle of this method is very straight forward. Two or more different objects is known in a global frame (NED or ECEF), with their difference in position giving a number of vectors in the global frame. Through the use of imagining sensors (i.e camera or sonar) strapped to the vehicle, the same vectors could be found relative to body-frame. The use of several vectors instead of just one, finding the rotation most agreeing to them all will give an estimate of even higher accuracy.

This method has been shown to give estimates with an accuracy down to 0.02° with multiple objects and sufficient base line between them, but also requires advanced sensors and processing power to utilize. It also requires two or more objects to be observed with known global positions.

Method 4: Vector from vehicle to external object

The essence of this method is quite similar to Method 3. The difference being that one of the objects are substituted with the vehicle itself. By knowing the global position of the vehicle and the global position of another (or several other) objects, the vector between them in the global frame is known. Then, the only thing remaining is to find the *bearing* to the observed object in body-frame, as the length of the vector is the same in both frames.

This method will usually also provide quite accurate results given a long distance to the measured object, but suffers an additional requirement to Method 3, in that it also needs to know the vehicle's global position.

Method 5: Body-fixed vector (Multi-antenna GNSS)

The method involves knowing the global position of two body-fixed points, usually through the use of a multi-antenna GNSS. As the two points are fixed in on the vehicle, the vector between them will always be assumed known in body-frame. The problem with this method comes from knowing the vector in the global frame with enough accuracy. An often limiting factor of this approach is the maximum distance from between the two points, i.e creating a sufficient baseline between them. If the baseline are too short, small inaccuracies in either position estimate will lead to large angle errors. It also relies on rigidity of the vehicle structure. If a part of the vehicle changes shape, the body-frame decomposition of the measured vector is no longer accurately known.

Method 6: Vehicle velocity vector

This is the method of comparing the velocity vector of the vehicle in both body- ($\boldsymbol{v}^b$) and global frame ($\boldsymbol{v}^n$). It is normally found in the global frame by using a position aiding sensor and calculate the velocity by using change in the position, or alternatively have GNSS Doppler velocity measurements available for more precise estimates. The velocity in body-frame is typically found by using sensors (camera, Doppler sensors) measuring relative velocity to external objects. It could also use knowledge about restrictions in the vehicle's movements, e.g. a rail-locked vehicle locking the body-oriented position to be almost exclusively in the forward direction, such that:

$$\boldsymbol{v}^b \approx \begin{bmatrix} x \\ 0 \\ 0 \end{bmatrix} \tag{4.8}$$

This method relies upon good aiding information about inertial position and/or velocity. With higher horizontal velocities comes higher angle accuracy, but that also will require a larger space to allow for such speed. The main issue with this method will usually be to find the velocity decomposed in body-frame, as it will require a potentially extra sensor if there is not sufficient restrictions to vehicle movement.

Method 7: Vehicle acceleration vector

This is a method quite similar to Method 6, but instead of the velocity vector, it is now its derivative which is in focus. Measuring the acceleration in the body system is trivial for any vehicle relying on inertial navigation, as they almost always carries strap-down accelerometers. The main difficulty is inferring the vehicle acceleration in global frame from its position over time. As the integrated acceleration from position is doubly integrated, it takes more time to accurately estimate acceleration than compared to the integrated velocity. This means that an acceleration needs to be present over time or make slow changes for its estimate to be accurate. A way around this problem would be to have Doppler velocity measurements available, as measuring $\boldsymbol{v}^n$ skips one integration step, and makes the acceleration estimate more responsive and able to distinguish noise.

The main advantage with this method is that the sensory package for basic measurements are usually available on most vehicles (accelerometers and position aiding). It will however require sufficient horizontal vehicle acceleration, which in turn requires enough space to maneuver. Its also possibly to increase the accuracy by adding measurements of $\boldsymbol{v}^n$

Mesurability of the different vectors

Going through the different possible vectors to measure, it becomes clear that some methods as infeasible due to either lack of sensor availability, dynamics of the multicopter or accuracy.

Method 1 will not be reliable for a multicopter that uses electrical engines, as the EM-noise created by the electric motors will constantly disrupt the magnetometer.

Method 2 is infeasible as high accuracy gyros are expensive, and using movement to cancel the biases puts restriction on the vehicle's mobility.

Method 3 requires imaging sensors and software, which would add to weight and cost. It is also not guaranteed that relative positions of objects in the global frame is is known, or that the objects are observable, at all time.

Method 4 suffers from much the same problems as Method 3, needing imaging sensors and software. It additionally needs aiding for position, which by introducing more measurements with additional measurements errors, reduces accuracy.

Method 5 could have been a viable option for larger multicopters. With a distance, called baseline, between the antennas of 0.5m, an accuracy of 0.2° could be achieved according to (Hem, 2017). This will however require a multi-antenna GNSS-receiver of a pretty hefty price ($\approx$ \$7000), as well as adding an additional kilo. It is also a completely unviable option for smaller multicopters, as shorter baselines give a too inaccurate measurement to produce accurate measurements.

Method 6 is normally a good alternative, as many vehicles driving in the same direction converges to a forward-only motion, removing any body-aligned sideways or vertical motion. Such knowledge of vehicle dynamics in cooperation with knowledge of roll and pitch (which could be found even in motion) would give e precise estimate of the body-aligned velocity even without any additional sensors. This is however not the case for a multicopter, as it could move in any direction independently of its heading, rendering this method inferior to Method 7.

Method 7 is the "safe choice" for any inertial navigation system in motion, in that it is reliable with some accuracy with basic sensors. This is a method that in Authors opinion should always be used to provide additional heading measurements for multicopter-based systems, as it under certain conditions during flight always will be able to provide semi-accurate heading estimates.

4.4 Suggested maneuvers to estimate heading

Three different approaches were tested for estimating the heading angle. All relied on a specific maneuver to be executed, which provided observability of a horizontal vector of sufficient length to the sensor package. The first approach was purely based on Method 7, while the third/second was arguably similar to both Method 5/Method 6, or Method 7. It should be noted that after consultation with the author of (Gade, 2016), it were concluded that it was based on Method 7, as it was the acceleration vector that was physically measured, giving observability to the heading angle.

All approaches will be preceded by a correction of roll and pitch, as they rely on freshly calibrated estimates of roll and pitch. It is therefore assumed that roll and pitch are known when trying to find heading.

Assumption 3: For all the heading measuring approaches, roll and pitch (ϕ, θ) are perfectly known quantities.

Succeeding the roll and pitch calibration, a maneuver consisting of horizontal acceleration in one direction followed by a quick stop is preformed to produce a large, persistent horizontal acceleration vector.

4.4.1 Approach 1: Compare acceleration vector directly

This approach uses the fact that a complete rotation could always be divided into three simple rotations, and knowing two of them makes it possible to find two vectors relating with a simple heading rotation.

Consider that

$$\boldsymbol{a}^n = \boldsymbol{R}_b^n(\boldsymbol{\Theta})\boldsymbol{a}^b = \boldsymbol{R}_z(\psi)\boldsymbol{R}_y(\theta)\boldsymbol{R}_x(\phi)\boldsymbol{a}^b \tag{4.9}$$

Doing this vector rotation in reverse gives us

$$\boldsymbol{a}^b = \boldsymbol{R}_b^n(\boldsymbol{\Theta})^\top\boldsymbol{a}^n = \boldsymbol{R}_x(\phi)^\top\boldsymbol{R}_y(\theta)^\top\boldsymbol{R}_z(\psi)^\top\boldsymbol{a}^n \tag{4.10}$$

Using the fact the both ϕ and θ are known quantities, introduction of the following reference frame will give vectors with our desired relationship.

$$\bar{\boldsymbol{a}}^b = \boldsymbol{R}_y(\theta)\boldsymbol{R}_x(\phi)\boldsymbol{a}^b = \boldsymbol{R}_z(\psi)^\top\boldsymbol{a}^n \tag{4.11}$$

where $\bar{\boldsymbol{a}}^b$ is the vector measured by the accelerometers, compensated for bias, roll and pitch. This is acceleration in what (Beard and McLain, 2012) has named "vehicle-1 frame ($\mathcal{F}^{v1}$)". The accelerometer biases wont be completely canceled, as they are estimated in NED, and transforming them back to body-frame will be slightly inaccurate as there are no guarantees for that the current heading estimate is accurate. It will however be assumed that the slight error originating from biases have no significant effect on the estimate.

Being able to produce the two vectors with the relationship

$$\boldsymbol{a}^n = \boldsymbol{R}_z(\psi)\bar{\boldsymbol{a}}^b \tag{4.12}$$

the only thing remaining is to find the angle between the two vectors.

Determining the angle from two vectors

Initially, there are two ways of finding the angle between two vectors. One way is to use that the inner product of two unit vectors is equal to the cosine of the angle between them

$$\frac{\boldsymbol{a}_h^n \cdot \bar{\boldsymbol{a}}_h^b}{||\boldsymbol{a}_h^n|| \cdot ||\bar{\boldsymbol{a}}_h^b||} = \cos\psi \tag{4.13}$$

where $\boldsymbol{a}_h$ refers to the horizontal components of the acceleration. This relation between the vectors is giving the heading angle by

$$\psi = \cos^{-1}\left(\frac{\boldsymbol{a}_h^n \cdot \bar{\boldsymbol{a}}_h^b}{||\boldsymbol{a}_h^n|| \cdot ||\bar{\boldsymbol{a}}_h^b||}\right) \tag{4.14}$$

This method could give information about the magnitude of ψ, but as the range of the *acos*-function is from 0 to π, it leaves no information about the sign of the angle.

The other way is to use the cross product, which will give the sine of the angle between the vectors.

$$\frac{\boldsymbol{a}_h^b \times \bar{\boldsymbol{a}}_h^n}{||\boldsymbol{a}_h^n|| \cdot ||\bar{\boldsymbol{a}}_h^b||} = \boldsymbol{n}\sin\psi \tag{4.15}$$

where $\boldsymbol{n}$ is the unit vector perpendicular to $\boldsymbol{a}_h^n$ and $\boldsymbol{a}_h^b$.

The problem with using the sine method, is that without any knowledge of the vector $\boldsymbol{n}$, a change of sign in the angle ψ would only result in $\boldsymbol{n}$ pointing in the opposite direction. This causes the *asin*-function of the left-hand side of (4.15) to only yield ψ in the range between 0 and $\frac{\pi}{2}$.

The solution to this problem comes from knowledge of the system. As both vectors used is in the horizontal plane, their cross product have to be perpendicular to the vertical z-axis. If the angle between the vectors are positive, the resulting vector, $\boldsymbol{n}$, will be pointing upward, while negative angles causes it to point downward.

Adding this information, one could form this relation between vectors and angle

$$\underbrace{\left|\left|\frac{\boldsymbol{a}_h^b \times \bar{\boldsymbol{a}}_h^n}{||\boldsymbol{a}_h^n|| \cdot ||\bar{\boldsymbol{a}}_h^b||}\right|\right|}_{|\sin\psi|} \underbrace{sgn(\boldsymbol{a}_h^b \times \bar{\boldsymbol{a}}_h^n \cdot \boldsymbol{z})}_{sgn(\sin(\psi))} = \sin\psi \tag{4.16}$$

Which could be simplified to

$$\psi = \sin^{-1}\left(\frac{\boldsymbol{a}_h^b \times \bar{\boldsymbol{a}}_h^n}{||\boldsymbol{a}_h^n|| \cdot ||\bar{\boldsymbol{a}}_h^b||} \cdot \boldsymbol{z}\right) \tag{4.17}$$

The problem with implementing either of these two method separately is both their limited range, and their local numerical instability. According to (Gade, 2010), tha *acos*-function is ill-conditioned for small angles, while the *asin*-function is ill-conditioned near $\pm\frac{\pi}{2}$ (and not valid above $\frac{\pi}{2}$). The best numerical accuracy will therefore be achieved by utilizing the *atan2*-function on both (4.14) and (4.17) into the expression

$$\psi = atan2\left(\underbrace{\frac{\boldsymbol{a}_h^b \times \bar{\boldsymbol{a}}_h^n}{||\boldsymbol{a}_h^n|| \cdot ||\bar{\boldsymbol{a}}_h^b||} \cdot \boldsymbol{z}}_{\sin\psi},\ \underbrace{\frac{\boldsymbol{a}_h^n \cdot \bar{\boldsymbol{a}}_h^b}{||\boldsymbol{a}_h^n|| \cdot ||\bar{\boldsymbol{a}}_h^b||}}_{\cos\psi}\right) \tag{4.18}$$

which will provide a well-conditioned angle with range from $(-\pi, \pi]$.

4.4.2 Approach 2: Find course(χ) and sideslip(β)

The second approach base itself on finding the heading angle by estimating course over ground and sideslip, and combining them according to

$$\psi = \chi - \beta \tag{4.19}$$

The course angle is found by using the horizontal components of the estimated velocity from the Kalman filter, $\hat{\boldsymbol{v}}^n$. Course over ground is the angle that the vehicle moves relative to the ground, i.e in the global frame. It could be estimated from $\hat{\boldsymbol{v}}^n$ in the following manner:

$$\chi = atan2(\hat{v}_y^n, \hat{v}_x^n) \tag{4.20}$$

The sideslip is however a more complicated matter. It requires, according to (Fossen, 2011, chapter 3), the velocity vector in the vehicle1-aligned system, and is defined by the following relation.

$$\beta = \sin^{-1}\left(\frac{\bar{v}_y^b}{\sqrt{(\bar{v}_x^b)^2 + (\bar{v}_y^b)^2}}\right) \tag{4.21}$$

where $\bar{\boldsymbol{v}}$ refers to $\boldsymbol{v}$ in the $\mathcal{F}^{v1}$-system, or for better range and numerical accuracy, use

$$\beta = atan2(\bar{v}_y^b, \bar{v}_x^b) \tag{4.22}$$

This will however require more advanced sensor which is not readily available to many navigation systems. It will therefore be proposed a method, using the maneuver's constant acceleration, to estimate vehicle1-aligned horizontal velocity through the horizontal acceleration in $\mathcal{F}^{v1}$, also known as $\bar{\boldsymbol{a}}_h^b$.

Reformulating equation (4.22) by using that $v = v_0 + a \cdot t$, gives that

$$\beta = atan2(\bar{v}_{y_0}^b + \bar{a}_y^b \cdot t, \quad \bar{v}_{x_0}^b + \bar{a}_x^b \cdot t) \tag{4.23}$$

Applying Equation (4.23) on the restrictions caused by our maneuver (no initial velocity, only horizontal acceleration in constant direction), leaves an even simpler equation ($\bar{\boldsymbol{v}}_0 = \boldsymbol{0}$).

$$\beta = atan2(\bar{a}_y^b, \quad \bar{a}_x^b) \tag{4.24}$$

The reasoning behind removing the multiplication with time is that only the direction of the horizontal velocity in $\mathcal{F}^{v1}$ matters, not its magnitude, and as the accelerations are suppose to be constant the direction will not change over time.

While this method in theory should give the sideslip the moment the acceleration starts, errors and disturbances needs to be suppressed. In order to achieve this, the following acceleration model is considered:

$$\boldsymbol{a} = \boldsymbol{a}_c + \boldsymbol{b}_d + \boldsymbol{\epsilon}_d \tag{4.25}$$

Where $\boldsymbol{a}_c$ is the commanded acceleration, $\boldsymbol{b}_d$ is the constant part of the disturbance and $\boldsymbol{\epsilon}_d$ is the zero-mean normally distributed noise.

Same as in Section 4.1, it is only the components in the horizontal plane and perpendicular to the vector actually being measured that will give error in the angle estimates.

The influence from the constant disturbance on the velocity will be counteracted by that it is present in acceleration at measurement time as well. The maneuver will not follow the planned path, but the changes will affect sideslip and course equally, making the heading estimate unaffected. The effect of the zero-mean noise over time on the horizontal velocity, $\boldsymbol{v}_h$, will be suppressed by the fact that $||\boldsymbol{v}_h||$ increases.

This means that Approach 2 is more accurate the longer the acceleration persists, as a longer velocity vector is less affected by small directional errors.

4.4.3 Approach 3: Comparing body-acceleration to change in position.

The idea of this approach is similar to Approach 2, where the direction of the velocity in body-frame is found by assuming constant acceleration in a body-system of non-changing orientation. This causes the horizontal direction of the acceleration in body to be equal to velocity's horizontal direction (in body-frame). The same could be said for the change of position in body-frame. The change of position in a non-changing body-frame will be the double integration of the body-aligned acceleration. If the acceleration in addition is constant, the direction of the position change in body-frame is the same as the direction of the acceleration. This is explained in the relation:

$$\angle_z \delta \boldsymbol{p} = \tan^{-1}\left(\frac{\overbrace{(p_{0_y} + v_{0_y} t + \frac{1}{2}a_y(t)\cdot t^2)}^{p_y(t)} - p_{0_y}}{\underbrace{(p_{0_x} + v_{0_x} t + \frac{1}{2}a_x(t)\cdot t^2)}_{p_x(t)} - p_{0_x}}\right) \tag{4.26}$$

where $\angle_z \delta \boldsymbol{p}$ is the horizontal angle of the vector describing the change in position, relative to North. With the assumptions of zero initial velocity and constant acceleration, this could be further reduced to

$$\angle \delta \boldsymbol{p} = \tan^{-1}\left(\frac{\frac{1}{2}a_y t^2}{\frac{1}{2}a_x t^2}\right)$$

$$\angle_z \delta \boldsymbol{p} = \tan^{-1}\left(\frac{a_y}{a_x}\right) = \angle_z \boldsymbol{a} \tag{4.27}$$

To find the heading angle, it will therefore be sufficient to compare the angle of the acceleration from the accelerometer measurements transformed to the $\mathcal{F}^{v1}$-frame, to the change of position in the global frame.

Chapter 5

Results

Many of the results presented in the thesis is found by performing large-scale Monte Carlo simulations, setting up larger automated tests in the simulation environment. This is done to get a feeling of how stochastic elements of the simulations affects the outcome, as well as finding the expected estimation performance with higher certainty. It should be noted that the results are limited by the simulation environments accuracy in imitating the real world.

For all the simulations, the pseudorange measurements are set to a precision of $\sigma = 0.1m$, and a measurement rate of 10Hz unless stated otherwise

5.1 Performance of roll and pitch angle correction

The test on how accurate the roll and pitch calibration method performs is done by giving the multicopter a stationary position to regulate on. This was done keeping in mind that even with offsets in attitude, the multicopter with its implemented regulator would come to rest, and therefore with zero roll and pitch, with a positional steady state error. The measured angles have been low-pass filtered (higher order) to remove some high-frequency noise. The results could be seen in Figure 5.1.

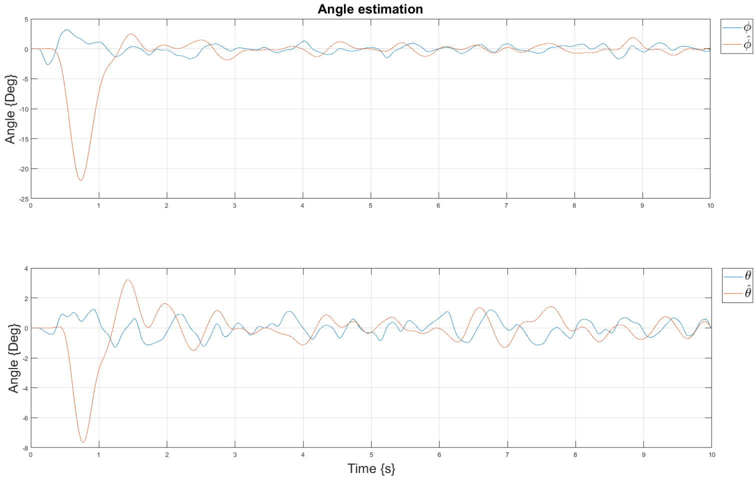

Figure 5.1: Plots displaying the angles ϕ (upper) and θ (lower), as well as their measured values according to Equation (4.6) that has been filtered.

The angles could be seen to fluctuate around zero degrees within the range of $\pm 2°$, but by assuming that the fluctuation is random and unbiased one could average the values of both the measured angles and the current angle estimate. The averaging of the estimate should only leave the estimate bias, while the average of the measured angles should leave approximately zero if done correctly.

If the averaging were done over an 8 second time period, the roll and pitch angle averages, $\bar{\phi}$, and $\bar{\theta}$,both came to zero with a mean averaging error of $\pm 0.04°$, and a standard deviation of $0.05°$. As the gyroscope is able to accurately track the angle velocity over short periods of time, the averaging of the estimated angles, $\bar{\hat{\phi}}$, and $\bar{\hat{\theta}}$, will result in only the biases plus the averaging error. Subtracting the averaged estimate values, when the real values are suppose to be zero, from the running estimate as calibration removes all biases except for the averaging error.

Considering all this, the resulting angle estimate after calibration will gives estimates of roll and pitch with expected errors of $\pm 0.04°$

5.2 Simulated heading measurements

Every simulation of multicopter flight performed the same type of operation. This operation consisted of the multicopter starting at the position $\boldsymbol{p} = [0, 0, 1]^\top$, before traveling rapidly to a new waypoint at $\boldsymbol{p} = [x_{path}, 0, 1]^\top$, where x_{path} varies between 2m, 8m and 20m. The movement of the multicopter was according to the autopilots response to waypoints, but was slightly underdamped by purpose to give a higher peak acceleration. Plots of the multicopter movement could be seen in Figure 5.2

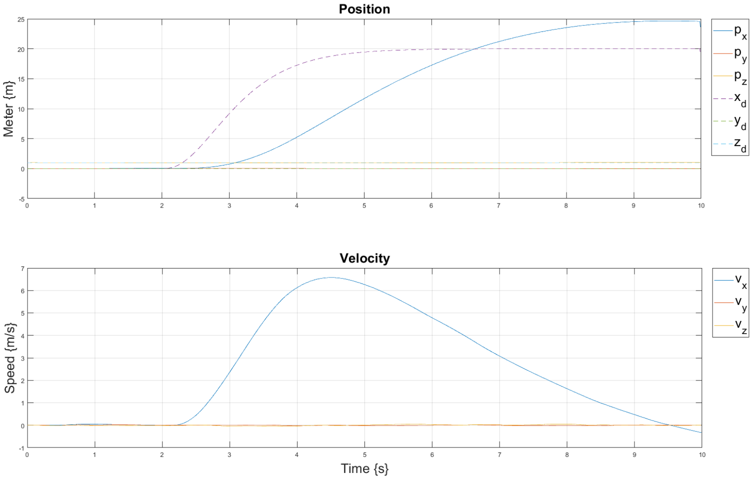

Figure 5.2: Position and velocity of the multicopter executing the maneuver for heading measurements

The multicopter remains stationary in the y- and z-direction, while the x-value goes to 20m before overshooting to 25m. Notice that the velocity is below zero at the end, indicating that it will move back towards x_d again. It's clear from both the velocity and the position that the movement is underdamped, but as only the time interval when the multicopter is accelerating forward is at interest, this will not influence the results. The reasons for this will be clarified in Section 5.2.2.

5.2.1 Continuous heading estimates:

The different approaches to heading estimation isn't as accurate at all time, due to either low acceleration, increased noise or other situations that increase the measurement errors of the two vectors to be compared.

Estimating heading using Approach 1:

Performing the the operation specified for heading estimation and doing post processing on sensor data according to the approach explained in Section 4.4.1, an estimates of heading angles was found for every timestep. This approach will also have the denotation a in most figures and equations, as it uses estimated acceleration in the global frame.

The estimated heading values are low-pass filtered with a discrete filter at the form

$$\begin{aligned} x_{lp}[k+1] &= x_{lp}[k] + \frac{1}{T}(x[k+1] - x_{lp}[k]) \\ x_{lp}[t_0] &= x[t_0] \end{aligned} \tag{5.1}$$

where x is the original signal, x_{lp} is the low-pass filtered signal, T is the time constant and t_0 is the filtration starting time. The time constant is set to 25.

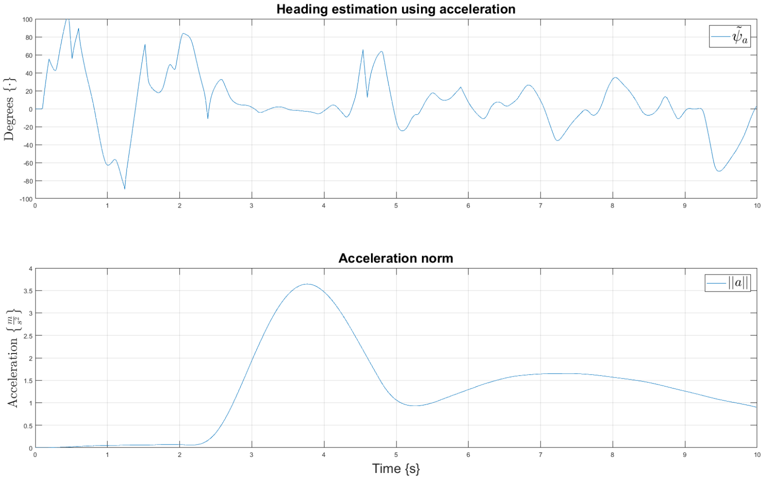

Figure 5.3: Plots showing the heading estimation error from the acceleration based estimation and acceleration norm over time. y-axis shows the range $[-100°, 100°]$

The resulting estimates could be seen in Figure 5.3, where the error is displayed together with the 2.norm of the acceleration. The norm is important as the norm of the horizontal acceleration is inversely proportional to the heading error, as explained by Equation (4.4). This can also be seen in the plot, as the error is at it smallest at time $t = 3.75s$, which is also close to the peak of the acceleration norm.

Estimate heading using Approach 2:

Doing post processing on sensor data according to the approach explained in Section 4.4.2, the heading estimates according to Approach 2 is found. The components of velocity-based heading estimation approach are the vehicle course over ground and the the sideslip. The estimates for the sideslip is low-pass filtered with a filter similar to the one described in Equation (5.1), but with a time constant $T = 2$. This approach will also have the denotation v in most figures and equations, as it uses estimated velocity in the global frame.

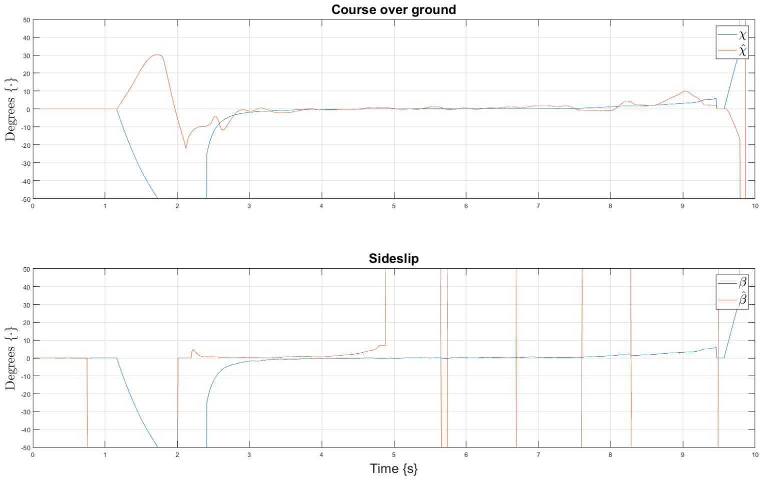

Figure 5.4: Plots of course (χ) and sideslip (β), as well as their measured counterparts. y-axis shows the range $[-50°, 50°]$

In Figure 5.4, the measured course and sideslip could be seen. Observe that sideslip is having huge fluctuations after $t = 4.5s$. This is because the equation for sideslip calculation assumes that the acceleration is constant and in the same direction as the velocity. When the multicopter starts to decelerate, the acceleration is in the opposite direction of the velocity, giving a sideslip estimation error of $\pm 180°$.

When the two components, sideslip and course over ground, is put together, the give a heading estimate. In Figure 5.5, the continuous measurements are shown. Notice that here as well, the estimation error is at its smallest when the acceleration norm peaks.

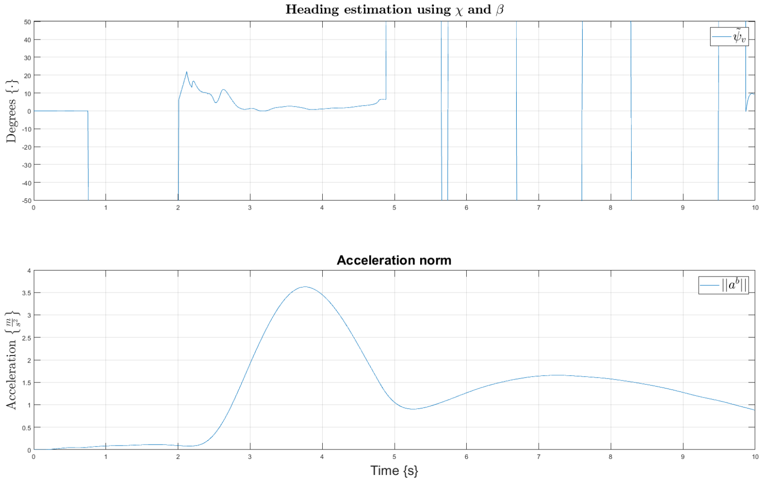

Figure 5.5: Plots showing the heading estimate error from the velocity-based estimation, as well as the acceleration norm over time. y-axis shows the range $[-50°, 50°]$

It is seen here that the heading estimation error follows the same fluctuations after $t = 4.5$ as were seen in the plot of vehicle sideslip. The sudden jumps between 180 and -180 is a result of the discontinuity in the $atan2$-function.

Estimating heading using Approach 3:

The final heading estimation approach compares the change in position to the position, as explained in Section 4.4.3. This is expected to be the most precise approach, as it only uses directly measured states, rather than indirectly measured ones through inference. The performance of the heading estimation is shown in Figure 5.6. This approach will also have the denotation p in most figures and equations, as it uses estimated position in the global frame.

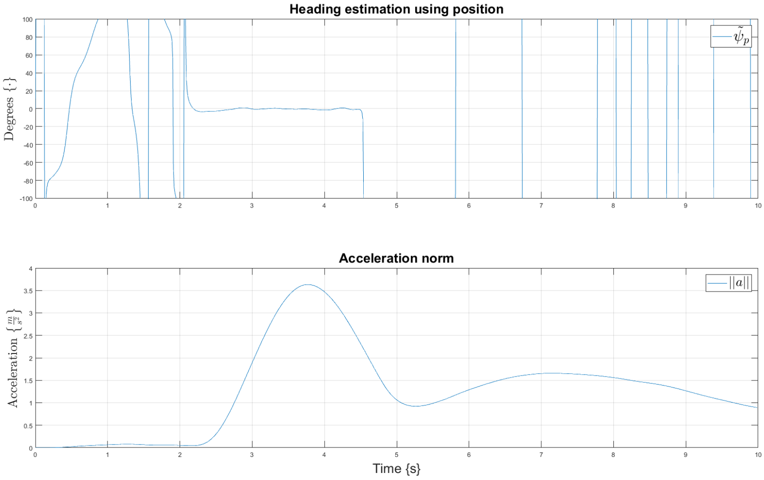

Figure 5.6: Plots showing the heading estimation error of the position-based estimation scheme, as well as the acceleration norm over time. y-axis shows the range $[-100°, 100°]$

The similarities between this and the two other approaches are clear, but there are two significant differences. The area of near-zero stability is, unlike in the other approaches, not centered around the acceleration norm peak. It is also of significantly higher accuracy, something that is not easily seen in the plots, but will be shown in later results. It should be noted that this approach has the same fluctuations as the velocity-based estimation scheme. It is caused by the same reason, which is the change in position being in the opposite direction of the acceleration when the vehicle decelerates.

5.2.2 Processing continuous heading estimations

The question that remains: how to create a single heading measurement from the entire maneuver? The solution could be to do the same to the raw data as was done with the roll- and pitch correction method. If an average over time are made on the continuous heading measurements, then measurement noise would be suppressed. The next question in then: which time intervals should be averaged?

Looking at the plots for the three different approaches for heading estimation, its clear than the time intervals has to be close to where the acceleration norm peaks. However, it is not clear how large the time interval should be, and it might be different for each methods.

First of all, it should be clear that only the time-interval with acceleration in positive x-direction is to be considered. This is solved with only targeting the time interval where the velocity norm increases, which could be described by

$$T_i = [0, t_v] \text{ where } t_v = [\, t \mid ||\boldsymbol{v}(t)|| = max(||\boldsymbol{v}(t)||) \,] \tag{5.2}$$

Furthermore, the averaging interval T_a, which is a subset of T_i, is found by taking all timesteps where the acceleration norm is within a certain percentage of the peak. Described in mathematical terms, it could be formulated:

$$\begin{aligned} T_a &= [\, t \in T_i \mid ||\boldsymbol{a}(t)|| >= k \cdot ||\boldsymbol{a}(t)|| \,] \\ k &\in [0, 1] \end{aligned} \tag{5.3}$$

where the optimal k is left to be found.

Optimizing the k-value

The next step is finding the optimal value of k for each of the three different approaches. This was done by using the Monte Carlo method, with 100 samples for each value of k between 0.5 and 1, with intervals of 0.01. Additionally, different combinations of GNSS-frequency and path length (denoted x_{path} in the begining of Section 5.2) were tested. Two GNSS-frequencies, $f = [100Hz, 10Hz]$ and three path lengths, $x_{path} = [2m, 8m, 20m]$, were tested in all their six different permutations. The results for optimal k-values are presented in Table 5.1.

	2m		8m		20m	
	100Hz	10Hz	100Hz	10Hz	100Hz	10Hz
a	0.78	0.61	0.89	0.99	0.92	0.96
v	0.94	0.99	0.94	0.99	0.99	0.99
p	0.63	0.50	0.58	0.51	0.64	0.66

Table 5.1: Table showing the optimal value for k for all three estimation schemes in six different scenarios.

Using these found values for all the different scenarios, a least squares method is used to find the optimal k-value for the three estimations schemes. This gives:

$$k^* = \begin{bmatrix} k_a \\ k_v \\ k_p \end{bmatrix} = \begin{bmatrix} 0.86 \\ 0.97 \\ 0.59 \end{bmatrix} \tag{5.4}$$

The difference between the mean error results before and after optimizing the k-value is significant, and will be presented in Section 5.2.3

5.2.3 Performance of the different estimation schemes at different heading angles

So far, every operation that has been presented had the multicopter at $\psi = 0$. The multicopter is able to fly in any direction independent of its heading angle. It would therefore be interesting to check the performance of the different estimation schemes at different angles, to see whether or not the expected reliability of the measurements should be dependent on heading state. The following results is produced by simulations using the Monte Carlo method. The simulation scheme consisted of six scenarios, the same as in Section 5.2.2. For every scenario, the simulations were performed when the multicopter was regulated to 49 evenly distributed heading angles between $-\pi$ and π. For each angle, 200 flights were performed, each which found a single heading measurement by averaging over the measurements over the time interval T_a, using the k^*, described in Equation (5.4). This results in a total of 58.800 simulations that each simulates ten seconds, with a time step $h = 0.01s$. It should be stated that these simulations required many ours of runtime, which is the reason for it not being too many of them.

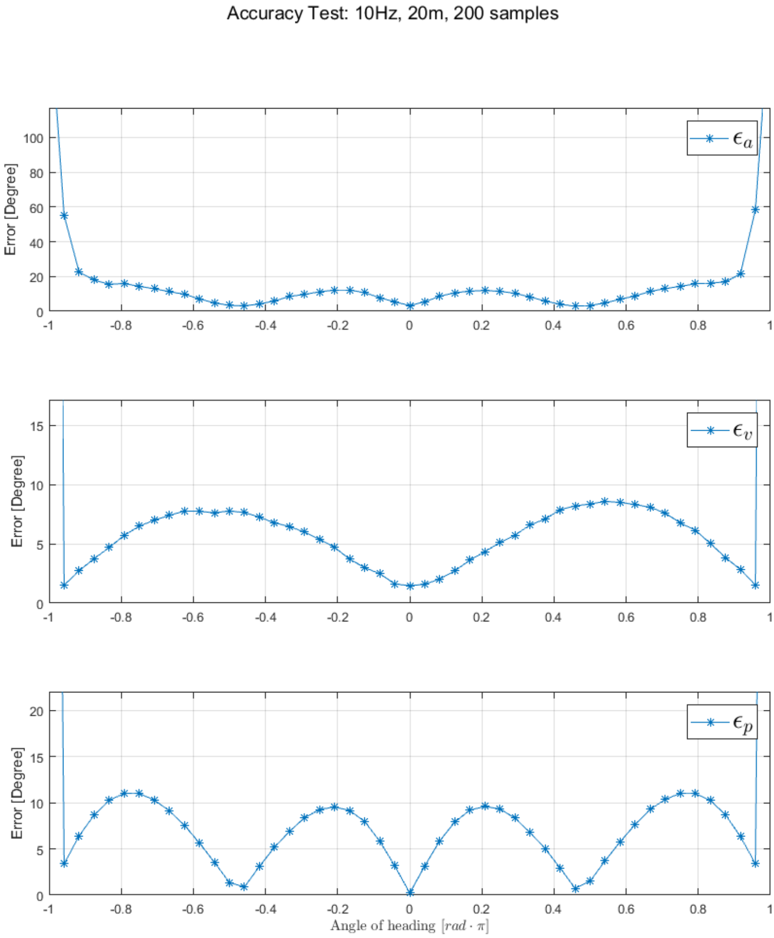

Figure 5.7: Plots displaying the mean estimation error in degrees when the operation is performed with $f = 10Hz$, and $x_{path} = 20m$. The three different plots show the three different measurement methods.

The results from the simulations shows that the heading state of the multicopter indeed is affecting the expected error of the heading measurements. As can be seen in Figure 5.7, both approach 1 and 3 is the most accurate in $\psi = 2n \cdot \frac{\pi}{4}$, and the least accurate at $\psi = (2n+1) \cdot \frac{\pi}{4}$. This is at least the case if one counts in the fact that every method is highly inaccurate around $\psi = \pi$, which is only a result of the discontinuity between $-\pi$ and π in the *atan2*-function. Approach 2 however differs from the others by that it is most accurate in $\psi = 2n \cdot \frac{\pi}{2}$, and the least accurate in $\psi = (2n+1) \cdot \frac{\pi}{2}$.

The results of all the simulations if shown in Table 5.2

	2m		8m		20m	
	100Hz	10Hz	100Hz	10Hz	100Hz	10Hz
ε_a	10.40°	23.63°	2.71°	7.12°	1.24°	3.26°
ε_v	5.02°	18.04°	1.22°	4.10°	0.44°	1.47°
ε_p	1.07°	2.38°	0.27°	0.57°	0.10°	0.21°

Table 5.2: Table showing the mean error found in simulations for each of the three approaches, for each of the six scenarios. The heading angle is set $\psi = 0$, and the numbers are provided in degrees of error

The plots of every simulation scenario could be found in Appendix D, showing Figures D.1-D.6 which present the results of the mean error of 200 simulations for each heading angle.

Improvement from k-value optimization

In Section 5.2.2, the optimization of the k-value were shown. It is therefore shown in Figure 5.8 the effects of the optimization with regards to the expected error. Comparisons with more detailed figures is found in Appendix D. The optimized results of the heading measurements error for each angle and every measurement approach is shown side by side with the results using the pre-optimized k-value in every measurement approach, which was $k = 0.90$. Only one of the six scenarios are shown, with GNSS-frequency $f = 100Hz$ and $x_{path} = 20m$. While this is the most realistic scenario, it shows the differences the best.

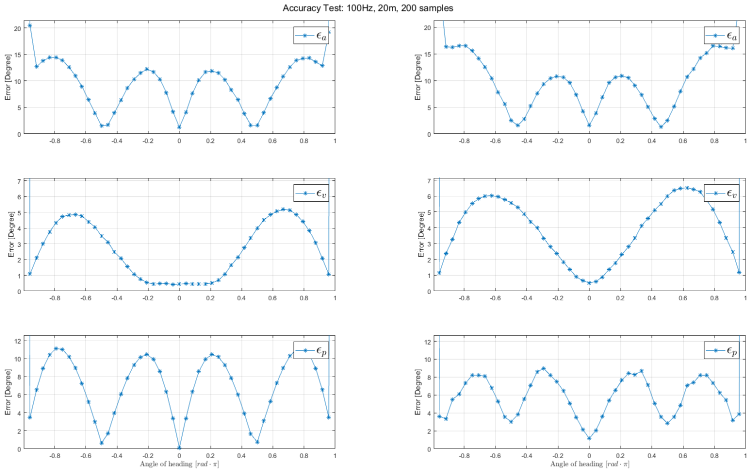

Figure 5.8: Plot of the heading measurement performance before (right) and after (left) k-value optimization. The methods from top to bottom are: a, v and p

The comparison shows that:

- The acceleration based method has a slightly improved best-case (around 0°), slightly worse around ±0.25 (±45°) and significantly better worst-case around ±0.75 (±135°).
- The velocity based method has a more robust best case area. It achieves best measurement accuracy in an area stretching from about -0.2 ($-35°$) to 0.2 (35°) in the optimized case, while only in 0 in the pre-optimized case. The worst case around ±0.75 (±135°) is also significantly improved, improving with over 1° in estimation error.
- The position based method experiences a trade-off. The best case accuracy, $\psi = 0°$, went from 1.15° to 0.10°. In the worst case angles, the accuracy is significantly worse, going from $\approx 8° - 9°$ to $\approx 11° - 12°$

Neither of the methods showed any signs of improving at the angles $\psi = \pm 1$ (±180°), which is to be expected.

5.3 Experimental results for heading estimation

Results presented in this section is calculated in post-processing from real flight data produced by a multicopter in an NTNU laboratory. The multicopter had 4-rotors, a state-of-the-art INS and received high-precision positional aiding from imaging sensors placed around in the laboratory. It should also be noted that the area of which the multicopter had to maneuver on was limited by the range of the position aiding system to a rectangular area of about $12m^2$. This is important because it restricts the intensity and duration of constant movements, which in the simulated case is equivalent to reducing x_{path}.

Figure 5.9 shows the multicopter at rest on the laboratory floor, right before flight.

Figure 5.9: Picture of the multicopter taken at the Motion-Capture laboratory at the Department of Engineering Cybernetics.

The following plots will show attitude estimation performance for all three methods. The time interval shown was the one best fulfilling the requirements for the suggested maneuver, that is, zero initial velocity and constant acceleration. It should be noted that heading error is calculated with the multicopter autopilot's angle estimates as the "true" angles, meaning that any estimation error could propagate to additive error in the measurements.

In Figure 5.10 it could be seen that the acceleration based measurement method is fairly accurate when the acceleration norm is relatively high and not rapidly

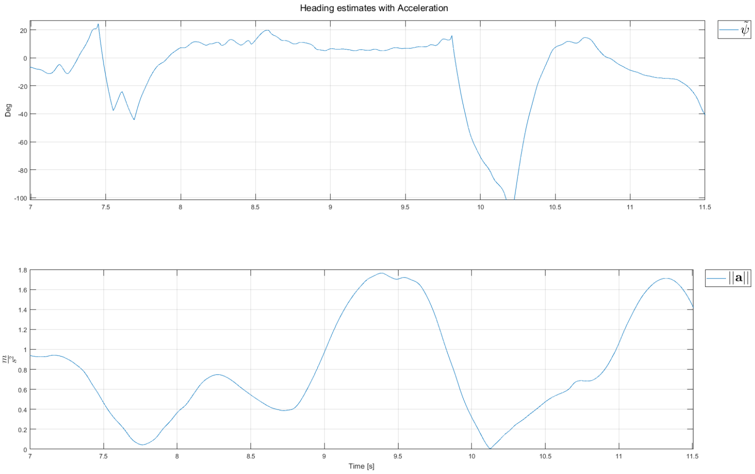

Figure 5.10: Plots of the heading measurements using the acceleration based method, together with the acceleration norm.

decreasing. It achieves an heading accuracy of about 8° − 10° when meeting the measurement conditions. The accuracy also plummets when the acceleration norm experiences a rapid decrease.

The plots in Figure 5.11 shows that the accuracy of the velocity based measurement method is not nearly as good as in the simulated case. It achieves at best and accuracy of $\approx 10^\circ$. There is however no visible correlation between the acceleration norm and the measurement accuracy, something that makes it hard to find conditions for when a high accuracy measurement could be taken using this method.

Figure 5.12 shows plots of the heading estimation using the position based measurement method. While estimation error is fairly low, it suffers from low correlation between estimation error and acceleration norm.

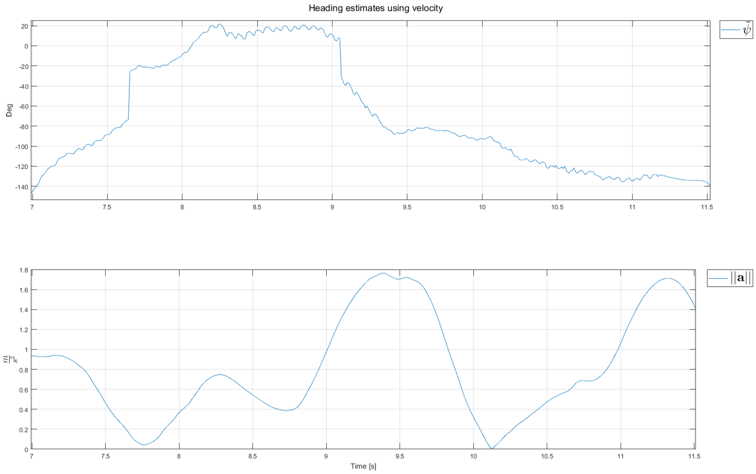

Figure 5.11: Plots of the heading measurements using the velocity based method, together with the acceleration norm.

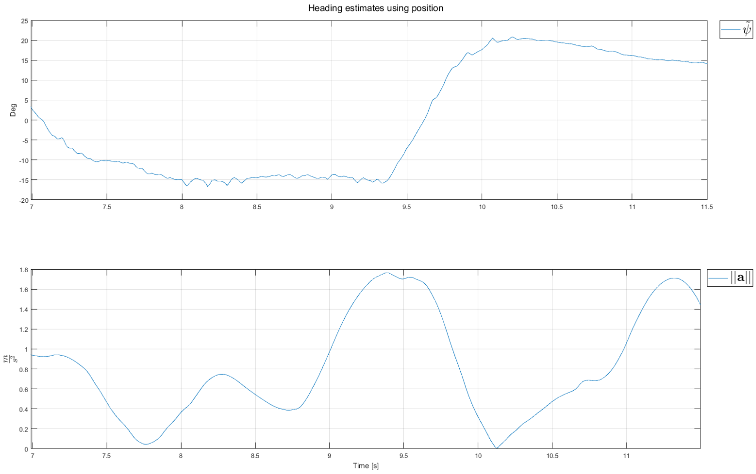

Figure 5.12: Plots of the heading measurements using the position based method, together with the acceleration norm.

Chapter 6

Discussion

This chapter will discuss the performance of the different measuring methods, theorizing about possible causes for their strengths and weaknesses. It will also put additional perspective to the differences between the real flights and the simulated ones, explaining why the accuracy of the results were so different.

6.1 Simulator

The performance of the simulator is more than good enough to test the different algorithms. Its simulated sensory packages are set to realistic accuracies, while the controller for the autopilot is simple, but effective. The autopilot is able to follow waypoints with controlled movements, staying within the acceleration- and velocity restrictions put on the multicopter.

The multicopter is at most able to produce a specific force of $\frac{G}{2}$ in any direction before its motors go into saturation, and achieve velocities of $25\frac{m}{s}$ before further acceleration in same direction is prohibited.

The visualizer was a great asset both when the simulator's autopilot had to be re-tuned for higher accelerations, and when the flight data from the real multicopter flight sequences were analyzed and ruled whether to be useful for post-processing or not.

6.2 Performance of roll/pitch estimation

The results from the roll- and pitch estimation using the gravity vector shows that it is able to produce highly accurate estimates. The dynamics of the multicopter also provides a method for checking integrity of the angle estimates by cross-checking it with estimated acceleration from position aiding sensors. If the vehicle experiences zero acceleration, this indicates that both roll and pitch must be zero. This means that even if one the accelerometers should fail, the inconsistency of the information from estimated inertial acceleration and accelerometer measurements warns the system that something is wrong, and estimates cannot be trusted.

In the simulator, the accuracy achieved of $\pm 0.04°$ over 8 seconds is well within the required accuracy of most operations, at least for the purpose of a multicopter. The angle estimates can however be further improved with an increased averaging duration.

6.3 Heading estimation

The heading estimation methods are producing accurate heading estimates under controlled circumstances with few spacial restrictions. The results presented in Table 5.2 show that if necessary initial conditions are met, estimates with an accuracy of less than 0.25° could be made if the maneuver is executed properly. It is also clear that both a longer traveling distance and higher GNSS frequencies drastically decreases the estimation error.

It must be emphasized that the stated accuracy is only achieved when $\psi = 0$, which raises the question: how does one guarantee that the maneuver is performed with zero heading angle when the heading estimate is not accurate? One solution could be to solve this problem with multiple steps.

By inspecting Figure 5.7 one could see that the worst possible estimation error case (except for $\varepsilon_{\hat{\psi}} = \pm 180°$) would be when $\varepsilon_{\hat{\psi}} = 45°$, as regulating $\hat{\psi}$ to zero would give $\psi = \pm 45°$ and give worst case estimation error. This will give an expected estimation error of approximately 10°. Regulating the new updated heading estimate to zero, the true heading angle is expected to really be in $\pm 10°$.

Performing a second heading measurement with the now improved estimate will give an expected measurement error of $\pm 3°$. Repeating the a few times, it can be shown that even in the worst case of initial heading estimation error, the estimation error will converge towards a final value, much lower than that of the first measurement. The final estimation error is defined by the measurement accuracy in $\psi = 0°$ and in worst case heading angle. This recursive measurement process will take much more time than a single measurement maneuver, something that is undesirable.

6.3.1 Heading estimation at non-zero heading

From the results seen in Appendix D, certain patterns of heading estimation error could be seen to appear in the results from all methods and measuring scenarios. The patterns are heading dependent, has amplitudes symmetric around zero heading, has defined peaks and dips, and varies from method to method. For the less accurate cases, such as the acceleration based method portrayed in Figure D.2, it might be hard to spot the symmetric error pattern. This is mainly because the added error from the curves is dominated by other error sources. The cause of this error patterns is unidentified.

A likely cause for the high error numbers seen around ±180° is the discontinuity in the *atan2*-function. Imagine that the heading of the multicopter is exactly 180°. Let also the measurement error be normally distributed around the real heading with an extremely high accuracy. As half the angle estimates will be right below real heading and the other half will be right above, the two halves are averaged for the sake simplicity of this example. This means that the average of the upper half of the estimates is $\hat{\psi}_+ = (180° + \epsilon)$ and the lower half is $\hat{\psi}_- = (180° - \epsilon)$, where ϵ is a positive constant determined by the spread of the error. As the range of the *atan2*-function is $(-180°, 180°]$, $\hat{\psi}_+$ exceeds the upper limit of the range (and therefore jumps down 360°) which gives it the new value $(-180° + \epsilon)$.

The average error of all the estimates will therefore be

$$\varepsilon_{\hat{\psi}} = \psi - \frac{1}{2}(\hat{\psi}_+ + \hat{\psi}_-) = \psi \tag{6.1}$$

This explains why the error around at $\psi = \pm 180°$ seems to be exactly 180°, which could be seen in Figure D.2. For the angles close to, but not exactly at ±180°, the error is high, but still lower than 180° as less than half of the randomly distributed estimates are on the wrong side of the discontinuity. As that portion decreases with the real heading's distance from the discontinuity, it makes sense that the average estimation error decreases as well.

6.3.2 Comparing the heading estimation methods

Remark: From now on and until the end of this section, the position based measuring method will be referred to as method 'p', the velocity base method as 'v' and the acceleration based method as 'a'.

From the results of the simulated heading measurements, there is no doubt that the zero-heading accuracy of method 'p' is the best, while the accuracy of method 'v' is superior to that of method 'a'. These differences are to be expected, because the vehicle's movement vectors $\boldsymbol{v}$ and $\delta\boldsymbol{p}$ are longer than $\boldsymbol{a}$ in the performed maneuver, creating smaller estimation errors. Another cause is that it takes more time to differentiate the real signal from the position aiding measurement noise for acceleration than for position and velocity, making the acceleration it less accurate.

The implementation of method 'a' is pretty straight-forward involving only a rotation using roll and pitch, followed by finding the angle between two vectors. The implementation of method 'v' is more of a challenge, as the heading estimate consists of two components. Both components had to be filtrated with time constants decreasing with an increasing horizontal velocity norm, and are found using the *atan2*-function. Implementation of method 'p' has about the same complexity as method 'a', with the only difference being that a starting position has to be found and subtracted from current position at every time step.

If the non-zero heading angles are to be considered as well, method 'p' is still the best, except for in the two scenarios where $x_{path} = 20m$. In those cases method 'v' has a lower worst case estimation error

Method '$\boldsymbol{a}$' as continuous measuring method:

Method 'a' does however have another significant advantage over the two other methods. It does not require any assumptions about the movement, other than that the vehicle accelerates. Both of the other two methods assume an acceleration of constant direction and yields very inaccurate heading estimates during a deceleration, caused by the vehicle's acceleration pointing in the opposite direction of its velocity. These inaccuracies are seen in Figure 5.5 and Figure 5.6.

This advantage means that method 'a' is well suited to provide continuous measurements of heading for an attitude observer. It would require the norm of horizontal acceleration, current heading estimate and roll- and pitch estimation error to calculate the measurement's reliability.

6.4 Experimental results:

Post-processing of the experimental flight data gives heading estimates of much lower accuracy than the simulated ones, with method *'p'* being the most accurate one. For method 'v', the large estimation errors could be explained partially by inaccurate estimates of roll and pitch affecting the transformation of $\boldsymbol{a}^b$ to the $\mathcal{F}^{v1}$-frame. The cause accounting for most of the error is however most likely that neither the conditions of constant horizontal acceleration direction or the starting conditions are fulfilled.

Method 'p' gives heading estimates with the lowest estimation errors, but only after manually picking the correct starting point to calculate $\delta\boldsymbol{p}$. There was no easy automatic way to find a suitable starting point for this method, leaving it in the same category as method 'v': mostly useful for controlled maneuver.

The estimation error shown in the results from method 'a' indicates high accuracy at high accelerations. At the first peak in acceleration norm, the average estimation error is approximately $6°$. The estimation error is nearly three times higher at the second peak of the acceleration norm, but that might be because there are acceleration in the z-direction present, making the norm of the horizontal acceleration appear larger than it really is.

Chapter 7

Conclusion

As a proof-of-concept testing, these heading measurement methods have proven able to produce heading measurement of a decent accuracy. It is clear that all the methods have their own usages, with the position- and velocity based methods being able deliver estimates of high accuracy under specific maneuvers and controlled circumstances, while the acceleration based method functions whenever the acceleration is high. The increased accuracy of the position aiding system in the form of increased pseudorange measurement frequency leads to significantly higher accuracy in the heading estimates as well.
See Table 5.2 for estimation error results.

The results from testing the heading measurement methods on an actual multicopter flight showed that while all the methods are effective when the maneuver is executed perfectly, the position- and velocity based methods are not very robust. Failing to do a perfect maneuver results in errors larger than expected. This holds especially true for the velocity-method, while the position-method saw constant, but moderate levels of estimation error.
See Figure 5.10-5.12 for estimation error results

An automatic method for producing a single improved measurement based on the horizontal acceleration norm proved to be possible. The use of averaging the heading measurements over a time interval dictated by the length of the horizontal acceleration grants the ability to smooth out random noise, leaving a more precise measurement. Optimization on when and how long this time interval should be in relation to the horizontal acceleration norm for each of the

methods will increase their accuracy rather than using a generically large time slot around the acceleration peak. An issue that the tests this project performed has showen is that when optimizing using data from only one vehicle heading angle (e.g $\psi = 0$), the optimization process actually worsens heading measurements when the vehicle is at heading angles other than zero.
See Equations (5.2), (5.3), (5.4) and Table 5.1 for relation between horizontal acceleration norm and averaging time interval.

The methods for estimation of roll- and pitch angles are already well documented to work well. The only error left in the estimates of the angles after performing averaged measurements using the gravity vector would be from biases in the accelerometers and residual error from random noise. The achieved accuracy in the simulations is more than well enough for the estimation error to be negligible in most cases relevant for the multicopter.
See Figure 5.1 for performance of roll/pitch measurements.

Chapter 8

Future Work

This chapter will provide suggestions on how to improve and develop further upon the results found in this thesis.

8.1 Attitude measurement for Kalman filter

The next step for the heading measurement methods would be to integrate them into a Kalman filter including attitude. As the methods are non-linear, this would require finding the jacobian of the measurement equations and finding suitable equations for calculating the reliability of each measurements (i.e calculating the elements of the R-matrix of the Kalman filter).

8.1.1 Roll- and pitch measurements

For the roll and pitch measurements, the gradient of the measurement equations (4.6) provides a relative clean jacobian. The measurement reliability weighting should be a constant value that originates from the accelerometer measurement noise, as well as a variable term coming from vehicle acceleration and estimation error in the accelerometer biases. The assumption made in Equation(4.6) and (4.7) is that the vehicle is not accelerated, so the norm of the vehicle acceleration (not including gravity) is a good indication for measurement reliability.

Two suggestions for ways of finding the vehicle acceleration norm could be

- Simply use the norm of $\hat{\boldsymbol{a}}^n$ found by the position aiding system. As this acceleration is found by observing the change of position over time, the gravity will not affect the estimate and only the vehicle acceleration will show. The disadvantage is however that a Kalman filter introduces a time delay to be able to distinguish the real acceleration from noise in the position measurements, of course depending on the measurement noise variance. This means that the found reliability of the measurement will actually be a little time-shifted from the measurement it is affecting.
- Use the norm of $\boldsymbol{a}^b_{imu}$. The coordinate system in which the measured vector is decomposed is irrelevant when calculating norms, so the measurements from the accelerometers will provide high-frequent acceleration norms with correct timing. One problem is that the accelerometer measurements does not sense only the vehicle acceleration, but also the gravity (which is fortunate, as this give observability of roll and pitch). One way around this issue could be to rotate the gravity to body system using current attitude estimates to cancel the about the gravity in the accelerometer. Using this method, the reliability of the measurements will be slightly inaccurate because of attitude estimation error.

8.1.2 Heading measurements

Of the heading measurement methods, the acceleration based one is best suited for a Kalman filter. The increased accuracy of the other methods is only obtainable because of the assumptions about constant direction of the acceleration and no initial velocity. These assumptions allows the use of longer measurement vectors, that according to Equation (4.4) reduces error in the heading estimate.

The jacobian of the acceleration based method's measurement equation will not be as nice as the ones for roll and pitch. The measurement equation for heading would be a slight modification of Equation (4.18):

$$\psi = atan2\left(\frac{(\bar{\boldsymbol{R}}\boldsymbol{a}^b_h) \times \boldsymbol{a}^n_h}{||\boldsymbol{a}^n_h|| \cdot ||\boldsymbol{a}^b_h||} \cdot \boldsymbol{z},\ \ \frac{\boldsymbol{a}^n_h \cdot (\bar{\boldsymbol{R}}\boldsymbol{a}^b_h)}{||\boldsymbol{a}^n_h|| \cdot ||\boldsymbol{a}^b_h||} \right) \tag{8.1}$$

where $\bar{\boldsymbol{R}} = \boldsymbol{R}_y(\theta)\boldsymbol{R}_x(\phi)$.

The derivatives of the measurement equation will be complicated, as the equation contains lots of nested functions.

The reliability values will be a bit easier to calculate as it would only be some function of horizontal acceleration length, roll- and pitch estimation error and measurement noise from both the accelerometers and position aiding systems.

8.2 Improving averaged heading measurement

There are two areas of the averaged heading measurement process that could greatly benefit from further development. Those are the planned trajectory of the maneuver, and the averaging time interval.

So far, the trajectory planning has come from positional PD-controller response to a set waypoint. The disadvantage of using this is that the multicopter uses just as much time slowing down as accelerating. When slowing down, the velocity- and position based measuring methods are useless since the accelerating direction is changed. A better maneuver would be to accelerate at a constant rate for most of the distance between $\boldsymbol{x}_0$ and $\boldsymbol{x}_{path}$, then rapidly decelerating at the last moment. This will allow for a longer effective traveling distance, which in turn increases the average accuracy of the measurements, as shown in Table 5.2.

The averaging time interval found in this thesis is described in Equation (5.4). However, as mentioned in the conclusion, these values were found from performing simulations at only zero heading angle. While testing the entire scope of possible heading angle might be unnecessary, there should at least be tests for the angles close to zero. The thought is that even when regulating the heading estimate to $\hat{\psi} = 0$ with some minor estimation error, the heading estimates should provide as accurate measurements as possible without having to resolve to the recursive method described in Section 6.3.

Finally, another area that should be investigated more concerning the averaged heading measurements is the angle-periodic estimation error curves. The origin of these errors has not been uncovered by the work done in this thesis, but it is suggested that other directions for maneuver paths are tried, so that it could be decided whether it is just the vehicle's heading or the angle between measured vector's two decompositions that dictated the error.

List of Tables

List of Figures

Appendix A

Geometric matrices

A.1 Rotation matrices

The rotation matrix $\boldsymbol{R}$ rotating between the two coordinate frames $\{a\}$ and $\{b\}$ is denoted as $\boldsymbol{R}_b^a$, is $SO(3)$, that is *special orthogonal group of order 3*:

$$SO(3) := \left\{\boldsymbol{R}|\boldsymbol{R} \in \mathbb{R}^{3\times 3}, \quad \boldsymbol{R} \text{ is orthogonal and } det(\boldsymbol{R}) = 1\right\} \tag{A.1}$$

The group $SO(3)$ is a subset of all *orthogonal matrices of order 3*, that is $SO(3) \subset O(3)$ where $O(3)$ is defined as

$$O(3) := \left\{\boldsymbol{R}|\boldsymbol{R} \in \mathbb{R}^{3\times 3}, \quad \boldsymbol{R}\boldsymbol{R}^T = \boldsymbol{R}^T\boldsymbol{R} = \boldsymbol{I}_3\right\} \tag{A.2}$$

A.1.1 Rotation matrix for Euler angles

The rotation from coordinate frame $\{a\}$ to coordinate frame $\{b\}$ is represented by the rotation matrix $\boldsymbol{R}_b^a$, which also represents the transformation of a vector in frame $\{b\}$ to frame $\{a\}$.

$$\boldsymbol{u}^a = \boldsymbol{R}_b^a\boldsymbol{u}^b \tag{A.3}$$

The rotation matrix is part of the This rotation is best described as a series of simple transformations around the principal axes in the order z, y, x with angles ϕ, θ, ψ.

The resulting matrix from this is

$$\boldsymbol{R}_b^a = \underbrace{\begin{bmatrix} \cos(\psi) & -\sin(\psi) & 0 \\ \sin(\psi) & \cos(\psi) & 0 \\ 0 & 0 & 1 \end{bmatrix}}_{\boldsymbol{R}_\psi} \underbrace{\begin{bmatrix} \cos(\theta) & 0 & \sin(\theta) \\ 0 & 1 & 0 \\ -\sin(\theta) & 0 & \cos(\theta) \end{bmatrix}}_{\boldsymbol{R}_\theta} \underbrace{\begin{bmatrix} 1 & 0 & 0 \\ 0 & \cos(\phi) & -\sin(\phi) \\ 0 & \sin(\phi) & \cos(\phi) \end{bmatrix}}_{\boldsymbol{R}_\phi}$$

$$\Rightarrow \boldsymbol{R}_b^n(\boldsymbol{\Theta}) = \begin{bmatrix} c\psi c\theta & -s\psi c\phi + c\psi s\theta s\phi & s\psi s\phi + c\psi c\phi s\theta \\ s\psi c\theta & c\psi c\phi + c\psi s\theta s\phi & -c\psi s\phi + s\theta s\phi c\phi \\ -s\theta & c\theta s\phi & c\theta c\phi \end{bmatrix} \tag{A.4}$$

A.2 Angular velocity transformation

The body-fixed angular velocity vector $\boldsymbol{\omega}^b = \boldsymbol{\nu}_2 = [p,\ q,\ r]^T$ and the Euler rate vector $\dot{\boldsymbol{\Theta}} = [\dot{\phi},\ \dot{\theta},\ \dot{\psi}]^T$ are not the same, but related through a transformation matrix $\boldsymbol{T}(\boldsymbol{\Theta})$ as

$$\dot{\boldsymbol{\Theta}} = \boldsymbol{T}(\boldsymbol{\Theta})\boldsymbol{\omega}^b \tag{A.5}$$

The difference between $\dot{\boldsymbol{\Theta}}$ and $\boldsymbol{\omega}$ is shown in Figure A.1, but is better described mathematically.

$$\begin{aligned} \boldsymbol{\omega} &= \dot{\psi} + \boldsymbol{R}_\psi\dot{\theta} + \boldsymbol{R}_\psi\boldsymbol{R}_\theta\dot{\phi} \\ \boldsymbol{\omega} = \boldsymbol{T}^{-1}(\boldsymbol{\Theta})\dot{\boldsymbol{\Theta}} &= \begin{bmatrix} 1 & 0 & -s\theta \\ 0 & c\phi & c\theta s\phi \\ 0 & -s\phi & c\theta c\phi \end{bmatrix} \begin{bmatrix} \dot{\phi} \\ \dot{\theta} \\ \dot{\psi} \end{bmatrix} \\ \Rightarrow \dot{\boldsymbol{\Theta}} = \boldsymbol{T}(\boldsymbol{\Theta})\boldsymbol{\omega} &= \begin{bmatrix} 1 & s\phi s\theta/c\theta & c\phi s\theta/c\theta \\ 0 & c\phi & -s\phi \\ 0 & s\phi/c\theta & c\phi/c\theta \end{bmatrix}\boldsymbol{\omega} \end{aligned} \tag{A.6}$$

We can clearly here see that there exists a singularity in $\theta = \pm\frac{\pi}{2}$, which is one of the main drawbacks with Euler angles

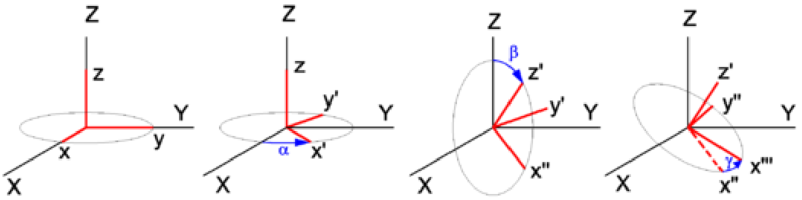

Figure A.1: Illustration of the difference between $\dot{\boldsymbol{\Theta}}$ and $\boldsymbol{\omega}$.
Source: (Citizendium, 2010)

A.3 Skew-symmetric matrix of a vector

A skew-symmetric matrix $\boldsymbol{M}$ is defines as

$$\boldsymbol{M}^T = -\boldsymbol{M} \tag{A.7a}$$

and has the property

$$\boldsymbol{u}^T \boldsymbol{M} \boldsymbol{u} \tag{A.7b}$$

for all $\boldsymbol{M} \in \mathbb{R}^{n \times 1}$ and $\boldsymbol{u} \in \mathbb{R}^{n \times 1}, \quad n \in \mathbb{N} \setminus \{0\}$

When working with vectors in three dimensional space, we can define the transformation of a vector to a skew symmetric matrix as

$$\boldsymbol{S}(\boldsymbol{u}) = \boldsymbol{S}\left(\begin{bmatrix} u_1 \\ u_2 \\ u_3 \end{bmatrix}\right) = \begin{bmatrix} 0 & -u_3 & u_2 \\ u_3 & 0 & -u_1 \\ -u_2 & u_1 & 0 \end{bmatrix} \tag{A.8a}$$

and has the property

$$\boldsymbol{S}(\boldsymbol{u})\boldsymbol{v} := \boldsymbol{u} \times \boldsymbol{v} \tag{A.8b}$$

Appendix B

Stability proof of attitude controller

Consider the system as described in 2.8. The angular controller is the following function of the Euler-angle error $\tilde{\Theta} = \Theta - \Theta_d$ and ω

$$\boldsymbol{\tau} = -\boldsymbol{S}(\boldsymbol{I}_b\boldsymbol{\omega})\boldsymbol{\omega} - \mathbf{K}_d\boldsymbol{\omega} - \boldsymbol{T}(\boldsymbol{\Theta})^\top \mathbf{K}_p\tilde{\Theta} \tag{B.1}$$

Using nonlinears system theory from (Khalil, 2002, Chapter 4) to show stability for the controlled system Choose the Lyapunov function candidate:

$$V = \frac{1}{2}\boldsymbol{\omega}^\top \mathbf{I}_b\boldsymbol{\omega} + \frac{1}{2}\tilde{\Theta}^\top \mathbf{K}_p\tilde{\Theta} \tag{B.2}$$

By deriving the derivative of the LFC, the systems stability could be analyzed:

$$\dot{V} = \boldsymbol{\omega}^T \mathbf{I}_b\dot{\boldsymbol{\omega}} + \tilde{\boldsymbol{\Theta}}\mathbf{K}_p\dot{\boldsymbol{\Theta}} \tag{B.3}$$

Using (2.8) and (B.1), it gives:

$$\begin{aligned} \dot{\boldsymbol{\omega}} &= \mathbf{I}_b^{-1}\boldsymbol{S}(\boldsymbol{I}_b\boldsymbol{\omega})\boldsymbol{\omega} + \mathbf{I}_b^{-1}\boldsymbol{\tau} && \text{(B.4)} \\ &= -\mathbf{I}_b^{-1}\mathbf{K}_d\boldsymbol{\omega} - \mathbf{I}_b^{-1}\boldsymbol{T}(\boldsymbol{\Theta})^\top \mathbf{K}_p\tilde{\Theta} && \text{(B.5)} \end{aligned}$$

and recalling from (2.7) that:

$$\dot{\boldsymbol{\Theta}} = \mathbf{T}(\boldsymbol{\Theta})\boldsymbol{\omega}^b \tag{B.6}$$

Which gives back in $\dot{V}$:

$$\begin{aligned}\dot{V} = &-\boldsymbol{\omega}^T\mathbf{I}_b\mathbf{I}_b^{-1}\mathbf{K}_d\boldsymbol{\omega} - \boldsymbol{\omega}^T\mathbf{I}_b\mathbf{I}_b^{-1}\boldsymbol{T}(\boldsymbol{\Theta})^\top\mathbf{K}_p\tilde{\Theta} &\text{(B.7)}\\ &+\boldsymbol{\omega}^T\mathbf{I}_b\mathbf{I}_b^{-1}\boldsymbol{T}(\boldsymbol{\Theta})^\top\mathbf{K}_p\tilde{\Theta} &\text{(B.8)}\end{aligned}$$

As any vector $\vec{a}$ is orthogonal with $(\vec{a} \times \vec{b})$ $\forall\vec{b}$, it results in:

$$\dot{V} = -\boldsymbol{\omega}^T\mathbf{K}_d\boldsymbol{\omega} \tag{B.9}$$

Notice that the Θ term of the Lyapunov function candidate canceled out the non-continuous term found in $\boldsymbol{\tau}$, which makes the functions V and $\dot{V}$ non-singular. If $\mathbf{K}_d > 0$ and $\mathbf{K}_p > 0$, we know that:

$$\left.\begin{array}{l} V \text{ is positive definite} \\ \dot{V} \text{ is negative semi-definite} \\ V \text{ is } \mathbf{C}^1 \end{array}\right\} \forall\boldsymbol{x} \in \{\boldsymbol{x} \in \mathbb{R}^6 \ \mid \ \boldsymbol{x} \neq 0\} \tag{B.10}$$

Krazovskii-LaSalle's Theorem states that if a Lyapunov function is radially unbounded and $\dot{V} \leq 0$ and:
Let M is the largest invariant $\in \Omega$ and:

$$\Omega = \{\boldsymbol{x} \in \mathbb{R}^n \ \mid \ \dot{V}(\boldsymbol{x}) = 0\}$$

If $M = \{\boldsymbol{x}_e\}$, then the equilibrium point $\boldsymbol{x}_e$ of the system is GAS
The regulated system has one equilibrium point, when $\boldsymbol{x} = 0$. This is also the only invariant set, as it is the only place where $\dot{\boldsymbol{\omega}} = 0$. The system is also radially unbounded (as it is a positive scalar function), and as earlier proven, $\dot{V} \leq 0$ $\forall x \neq 0$.
It can therefore from the Krazovskii-LaSalle's theorem be concluded that the angular control law makes the system GAS.

Appendix C

Proof for rank of sum of outer product

Consider the matrix $\boldsymbol{M} \in \mathbb{R}^{n \times n}$:

$$\boldsymbol{M} = \sum_{i=1}^{m} \boldsymbol{v}_i \boldsymbol{v}_i^T \tag{C.1}$$

where $\boldsymbol{v}_i \in \mathbb{R}^n \;\; \forall i$. Lets assume that $m \geq n$ and that there are at least n linearly independent vectors $\boldsymbol{v}_i$. This means that:

$$\begin{bmatrix} \boldsymbol{v}_1 & \boldsymbol{v}_2 & \dots & \boldsymbol{v}_m \end{bmatrix}^T \cdot \boldsymbol{x} \neq \vec{0} \quad \forall \boldsymbol{x} \neq 0 \in \mathbb{R}^n$$

This is one of the definition of a matrix with full rank, that its null-space is empty. Testing the same thing on $\boldsymbol{M}$, that is it is not full rank, it has to have a non-empty null-space:

$$\begin{aligned} \boldsymbol{M}\boldsymbol{x} &= \sum_{i=1}^{m} \boldsymbol{v}_i \boldsymbol{v}_i^T \boldsymbol{x} \\ &= \sum_{i=1}^{m} \boldsymbol{v}_i c_i \end{aligned} \tag{C.2}$$

Considering that the values c_i is the elements of the resulting vector of $[\boldsymbol{v}_1 \;\; \boldsymbol{v}_2 \;\; \dots \;\; \boldsymbol{v}_m]^T \boldsymbol{x}$, it is obvious that there exists a c_i which is non-zero regardless of $\boldsymbol{x}$. Using this, it gives

$$\boldsymbol{M}\boldsymbol{x} \neq \vec{0} \qquad \forall \boldsymbol{x} \in \mathbb{R}^n \tag{C.3}$$

This finally gives the result

If the vectors $\boldsymbol{v}_i \in \mathbb{R}^n$ *for* $i \in [1, 2, \ldots, m]$, *span a* n*-dimensional space, then the following equivalence holds, then the sum of its outer products will always be non-singular.*

Appendix D

Additional heading estimation plots

This appendix will present plots with the all the results discussed in Section 5.2.3.

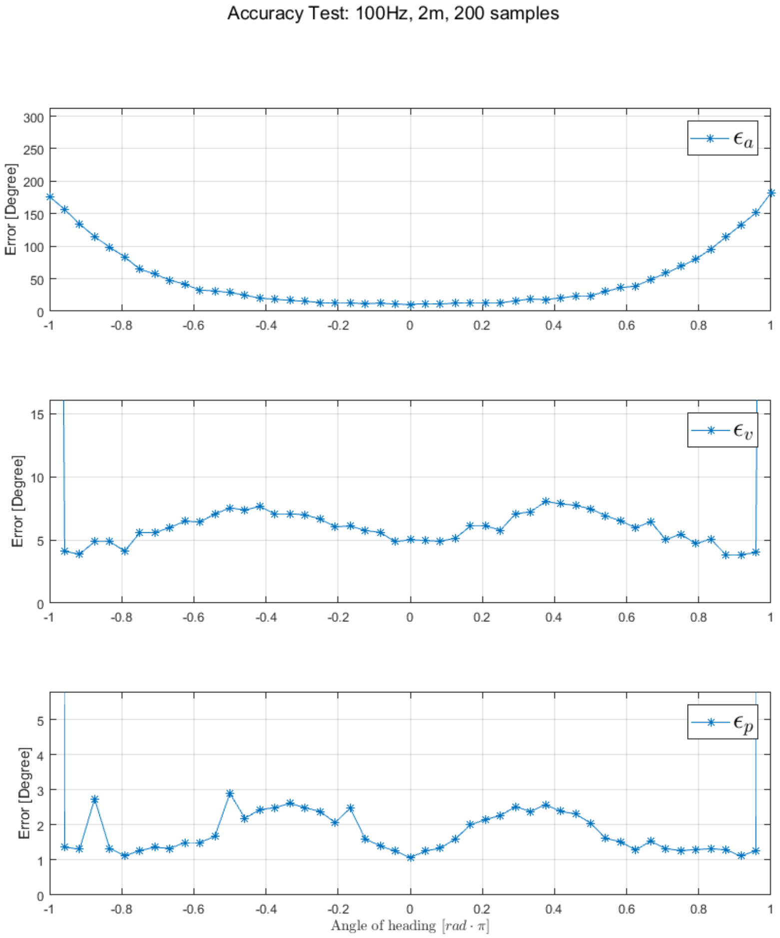

Figure D.1: Plots displaying the mean estimation error in degrees when the operation is performed with $f = 100Hz$, and $x_{path} = 2m$

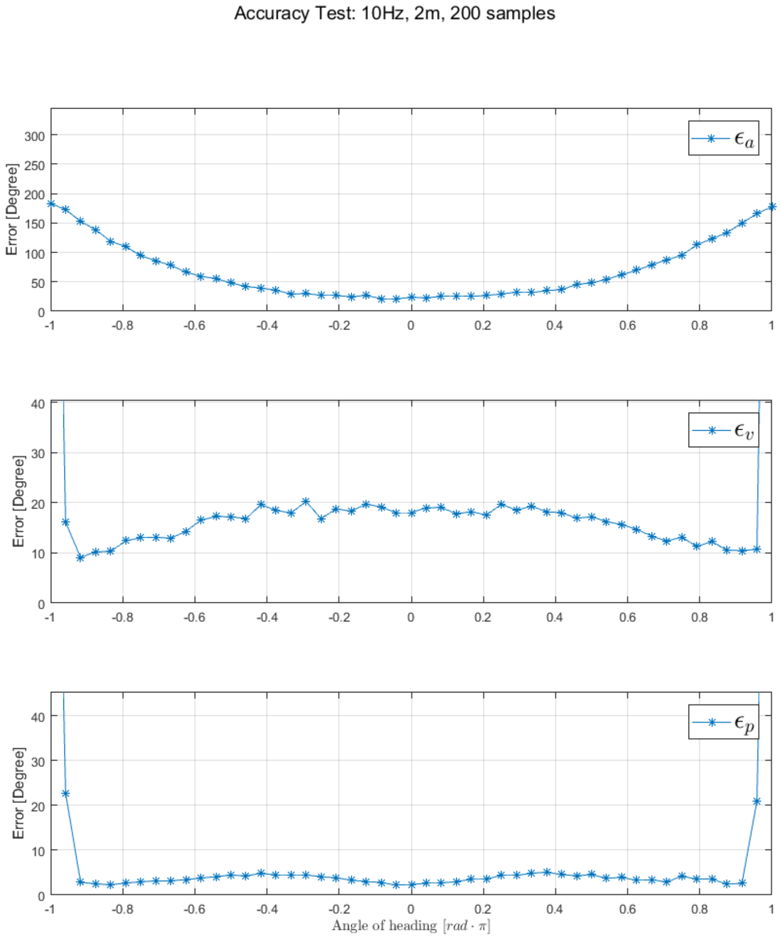

Figure D.2: Plots displaying the mean estimation error in degrees when the operation is performed with $f = 10Hz$, and $x_{path} = 2m$

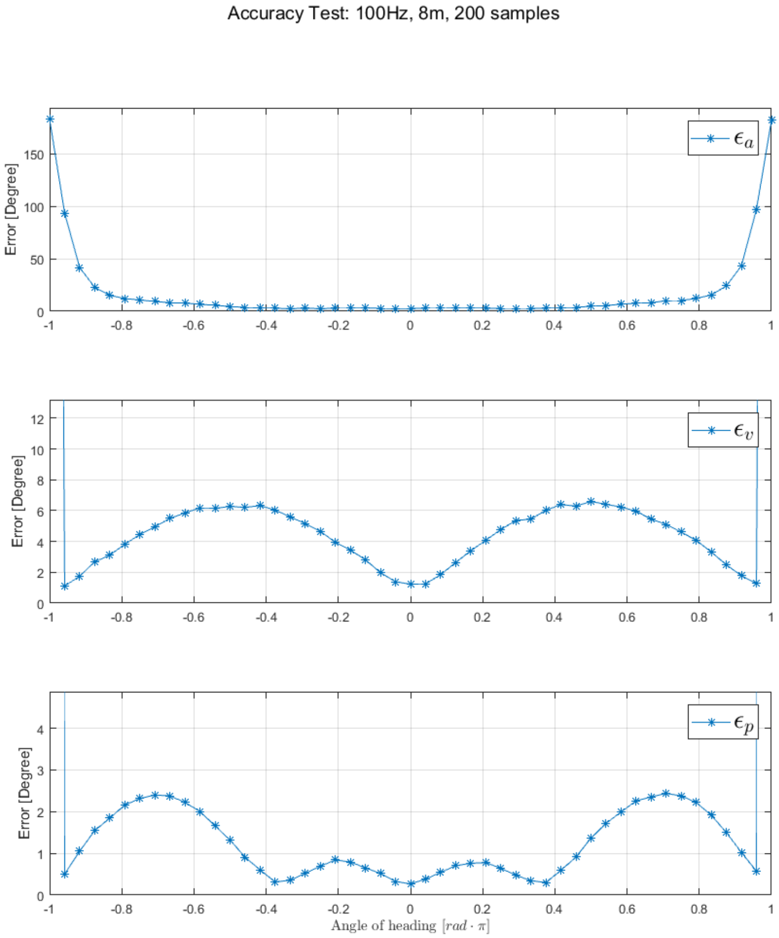

Figure D.3: Plots displaying the mean estimation error in degrees when the operation is performed with $f = 100Hz$, and $x_{path} = 8m$

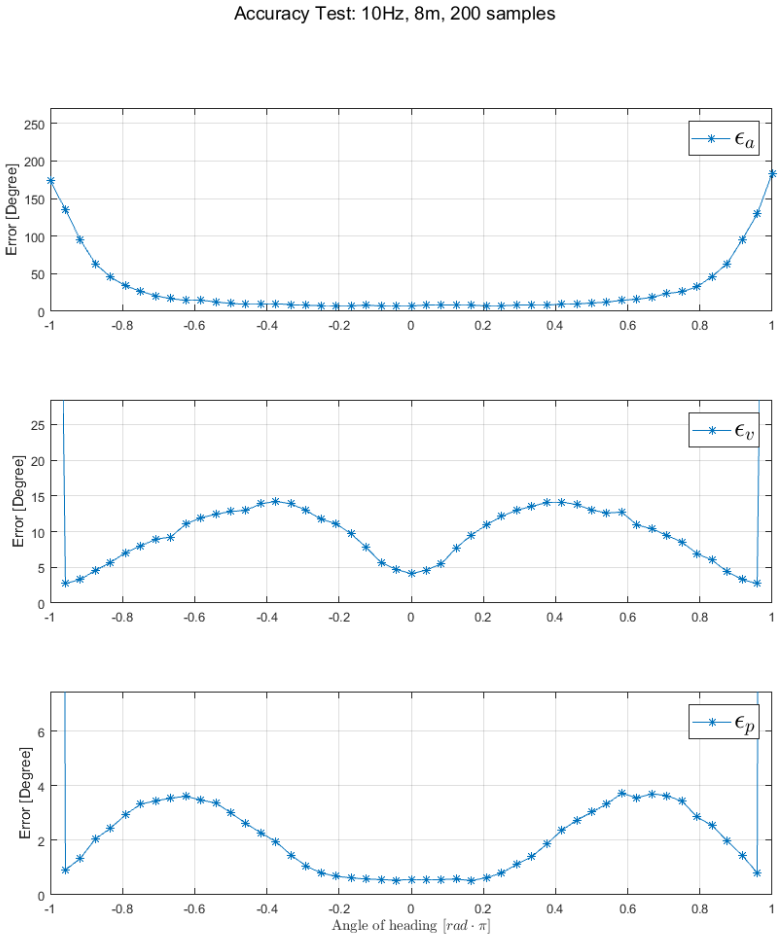

Figure D.4: Plots displaying the mean estimation error in degrees when the operation is performed with $f = 10Hz$, and $x_{path} = 8m$

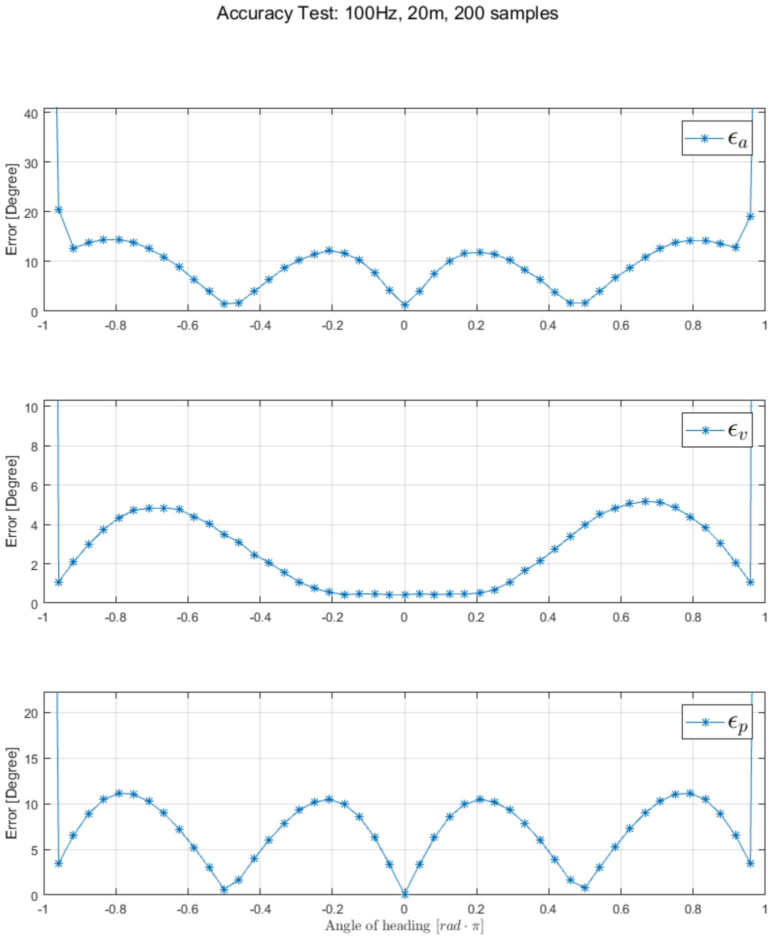

Figure D.5: Plots displaying the mean estimation error in degrees when the operation is performed with $f = 100Hz$, and $x_{path} = 20m$

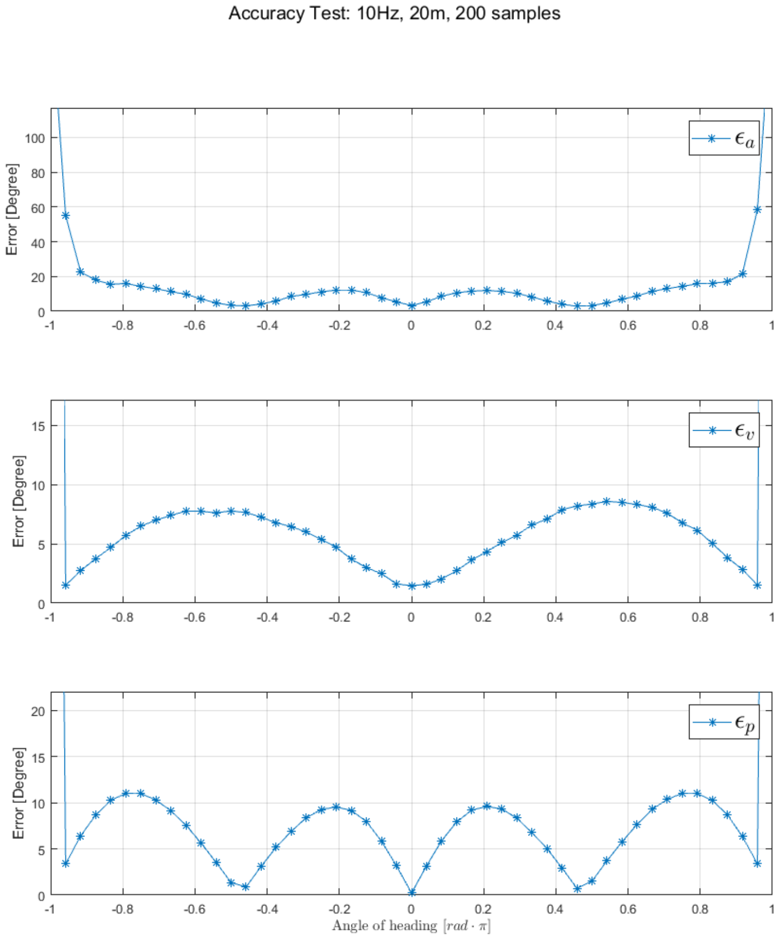

Figure D.6: Plots displaying the mean estimation error in degrees when the operation is performed with $f = 10Hz$, and $x_{path} = 20m$

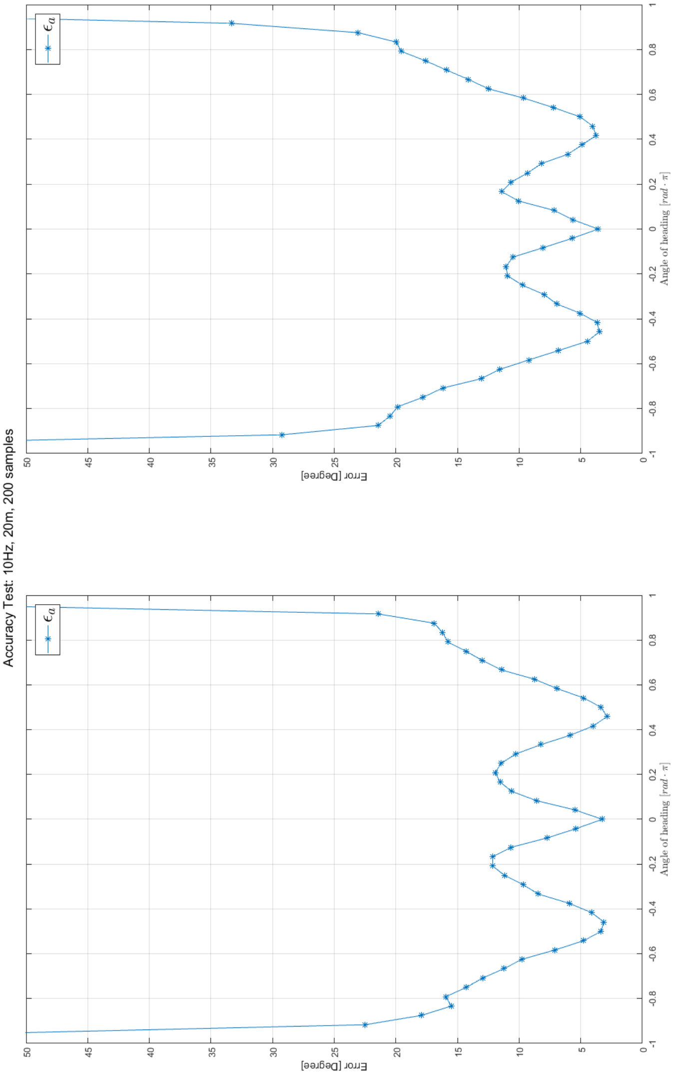

Figure D.7: Plots displaying comparison between pre- and post-optimized acceleration based heading estimation over different angles

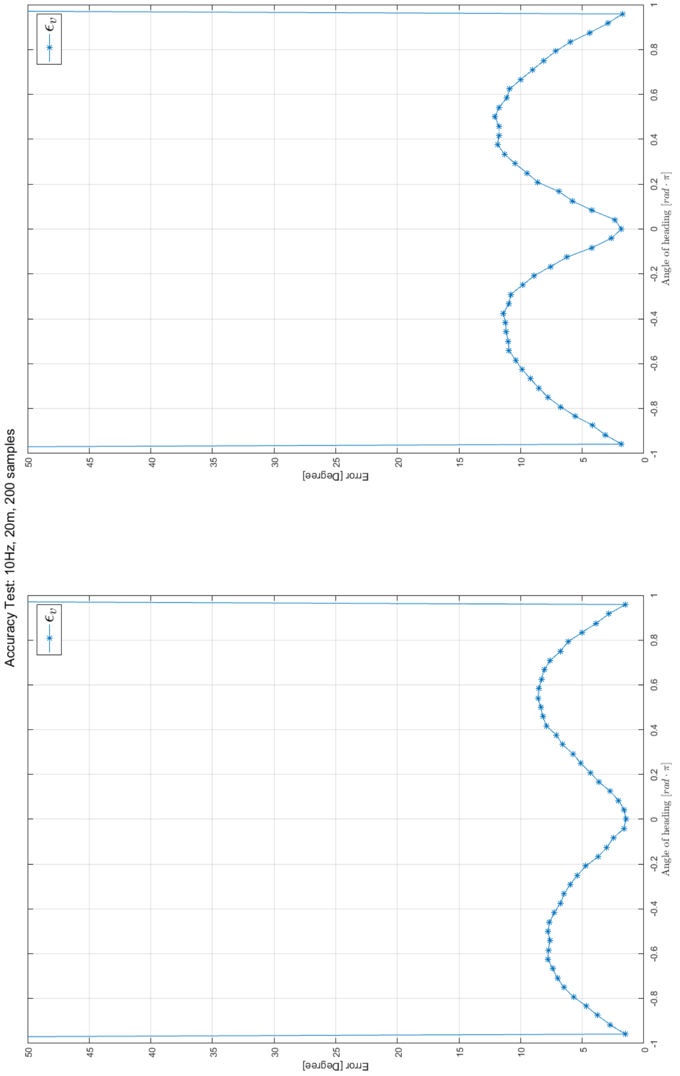

Figure D.8: Plots displaying comparison between pre- and post-optimized velocity based heading estimation over different angles

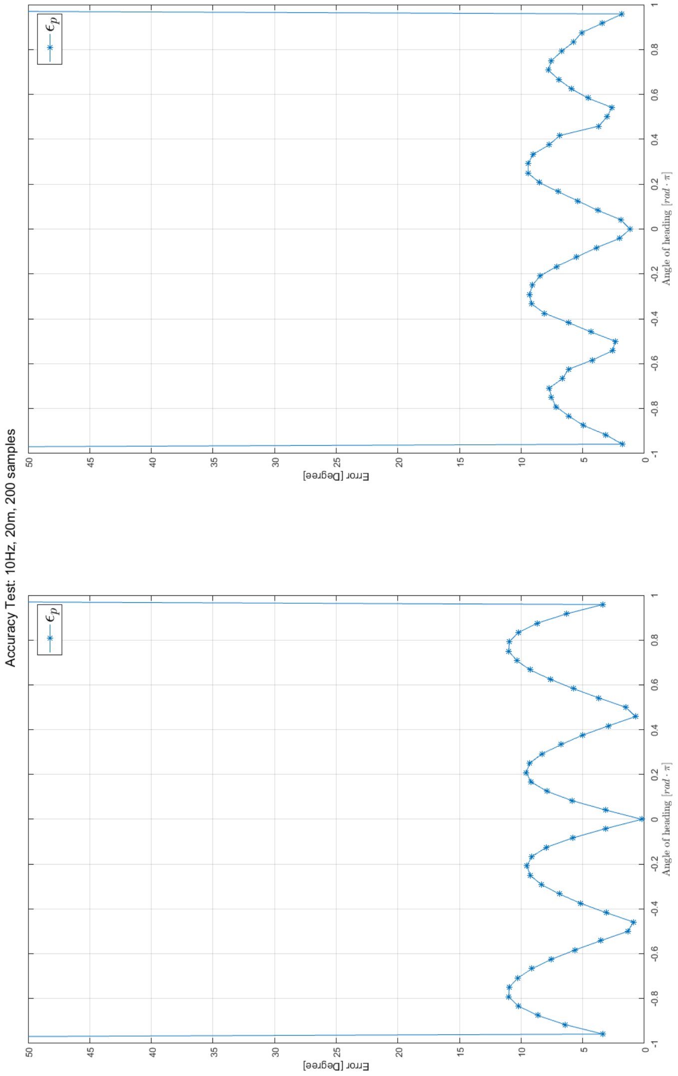

Figure D.9: Plots displaying comparison between pre- and post-optimized position based heading estimation over different angles

Appendix E

Matlab Code

All MatLab code is submitted as digital appendix. The code is written in Matlab17, and should be executable (run ”test_accuracy.n”) after the folder ”gnc” is included to path. With some small modifications to ”helicopter_init.m” (flick some of the switches in code) and ”Simulation_quadcopter_3DOF.n”, ”Simulation_quadcopter_3DOF.n” could be run to see plots and visualization of flight.

Experimental flight data will not be runable, as the flight data itself is excluded from the digital appendix.

Bibliography

Jens G. Balchen, Trond Andresen, and Bjarne A. Foss. *Reguleringsteknikk.* Department of Engineering Cybernetics, NTNU, 2003.

Paul Baltzer. *Das Extended Kalman Filter einfach erklärt*, 2013. `http://www.cbcity.de/das-extended-kalman-filter-einfach-erklaert` [Accessed 2018-05-29].

Randal W. Beard and Timothy W. McLain. *Small Unmanned Aircraft: Theory and Practice.* Princeton University Press, 2012.

Robert Grover Brown and Patrick Y.C. Hwang. *Introduction to Random Signals and Applied Kalman Fitlering.* Wiley, 2012.

Citizendium. *Euler Angles*, 2010. `http://en.citizendium.org/wiki/Euler_angles` [Accessed 2018-06-13].

Olav Egeland and Tommy Gravdahl. *Modeling and Simulation for Automatic Control.* Marine Cybernetics, 2002.

Jay A. Farrell. *Aided Navigation: GPS with High Rate Sensors.* Electronic Engineering, 2008.

T. I. Fossen and T. Perez. Marine systems simulator (mss), 2004. URL `http://www.marinecontrol.org`. Last visited 2016-12-12.

T.I. Fossen. *Handbook of Marine Craft Hydrodynamics and Motion Control.* John Wiley & Sons, 2011.

Kenneth Gade. A non-singular horizontal position representation. *The Journal of Navigation*, 2010.

Kenneth Gade. The seven ways to find heading. *The Journal of Navigation*, 2016.

Douglas Harper. *Etymology on Navigation*, 2018. `https://www.etymonline.com/word/navigation` [Accessed 2018-06-02].

Elder M. Hemerly, Benedito C.O. Maciel, Anderson de P. Milhan, and Valter R. Schald. Attitude and heading reference system with acceleration compensation. *Aircraft Engineering and Aerospace Technology*, 2012.

VECTOR VS330 GNSS Compass. Hemisphere GNSS, 8 2017. URL `https://hemispheregnss.com/Products/Products/Position-Heading/vector-vs330e284a2-gnss-compass-94`. Last visited 2018-05-27.

Petros A. Ioannou and Jing Sun. *Robust and Adaptive Control.* Dover Publications, 2012.

Tor A. Johansen and Thor I. Fossen. Nonlinear observer for tightly coupled integration of pseudorange and inertial measurements. *IEEE Transaction on Control Systems Technology*, 2016.

Tor A. Johansen, Jakob M. Hansen, and Thor I. Fossen. Nonlinear observer for tightly integrated inertial navigation aided by pseudo-range measurements. *Journal of Dynamic Systems, Measurement and Control*, 2017.

Hassan Khalil. *Nonlinear Systems.* Pearson, 2002.

Kristian Klausen. *Coordinated Control of Multirotors for Suspended Load Transportation and Fixed-Wing Net Recovery.* Department of Engineering Cybernetics, NTNU, 2017.

Heekwon No, Am Cho, and Changdon Kee. Attitude estimation method for small uav under accelerative environment. *The Journal of Global Navigation Satellite Systems*, 2014.

PBS Public Broadcasting Service. *PBS - Elmer Sperry*, 2018. `http://www.pbs.org/wgbh/theymadeamerica/whomade/sperry_hi.html` [Accessed 2018-06-03].

Elmer Sperry. *Gyroscope, Patent US1279471A.* Sperry Gyroscope Company, 06 1911. URL `https://patents.google.com/patent/US1279471`. Last visited 2018-06-2.

Bjørnar Vik. *Integrated Satellite and Inertial Navigation Systems.* Department of Engineering Cybernetics, NTNU, 2014.